Picking up a Soft 3D Object by "Feeling" the Grip

Huan Lin Feng Guo Feifei Wang Yan-Bin Jia
Department of Computer Science
Iowa State University
Ames, IA 50011, USA
linhuan,fguo,wangff,jia@iastate.edu

Abstract

This paper describes a strategy for a robotic hand to pick up deformable 3D objects on a table. Inspired by human hand behavior, the robotic hand employs two rigid fingers to first squeeze such an object until it "feels" the object to be liftable. Such "feeling" is provided by a (virtual) liftability test that is repeatedly conducted during the squeeze. Passing of the test then triggers a lifting action. Throughout the manipulation the object's deformation and its state of contact with the fingers and the table are being tracked based on contact events. Deformable modeling uses the finite element method (FEM) while slip computation employs the homotopy continuation method to determine the contact displacements induced by finger movements. Experiment was conducted for everyday items ranging from vegetables to a toy. A simulation-based comparison between deformable grasping and rigid body grasping reveals why soft objects are easier to pick up than hard ones, and demonstrates how a rigid body grasping strategy may fail on soft objects in certain situations.

KEY WORDS — Deformable grasping, gravity, liftability test, contact modes, finite element method.

1 Introduction

The human hand is experienced at manipulating soft objects in the daily life. For instance, to pick up such an object from a table, the hand usually squeezes it first with two or more fingers to achieve a firm grip. The squeeze is sometimes downward against the table in order to leverage its support to stabilize the object during the action, and to generate large enough contact areas to provide the needed friction. While squeezing the object, the fingertips are feeling its weight as well as the firmness of their grip to decide when to lift it. Once a lift starts, the hand may also apply some extra squeeze to prevent possible slips.

Inspired by the above squeeze-and-lift behavior, in this paper we introduce a strategy for a robotic hand to pick up deformable 3D objects resting on a table (modeled as a horizontal plane), using two rigid fingers with no force or tactile sensing capability. As illustrated in Figure 1, the two fingers $\mathcal{F}_1$ and $\mathcal{F}_2$ are initially placed at two locations on the object that would achieve "force closure" with the table contact if the object were rigid. This will prevent any possible rigid body movement of the object (so it can only deform) once the squeeze starts. The fingertips then begin to squeeze the object slightly downward against the table. The growing contact areas further constrain the object from any rotation or translation. After every extra amount of squeeze, a virtual liftability test is performed to estimate the progress in terms of the "portion of the object's weight that can be lifted up". Once the test is passed, both fingers switch to upward translations to lift the object off the table.

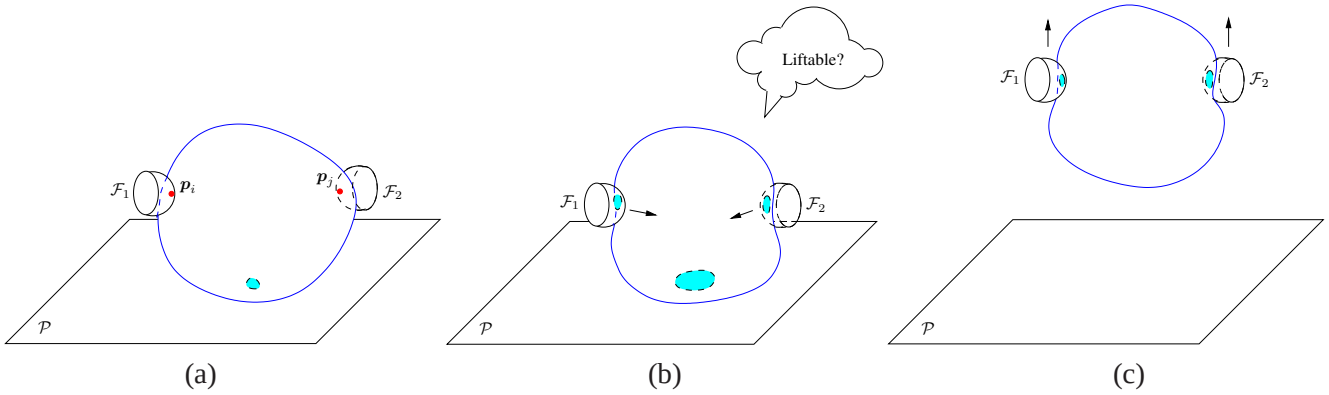

Figure 1: Lifting a deformable object off a horizontal supporting plane $\mathcal{P}$: (a) initial configuration and finger placement; (b) squeezing (with repeated liftability tests); and (c) liftoff. Contact regions are shaded.

The pickup strategy may perform a model-based simulation before the robot execution, or proceed with both simultaneously. For simplicity, we consider straight translations by the fingertips during the squeeze and upward translations during the lift. Robot execution becomes rather straightforward if knowing the initial finger contacts, the squeeze directions and the relative speed of the finger movements, and when to switch from squeezing to lifting. Finger contacts and squeeze directions are easy to specify as we will see. The squeeze-to-lift transition will depend on the outcome of the liftability test, which will be part of simulation.

The main technical difficulty of the strategy will thus come from model-based simulation. It is important to be able to track the object's shape and contact configuration (including contact modes) during the squeeze and lift operations. For this we will draw upon our recent work (Jia et al., 2014) on squeeze grasping of deformable 2D objects. One idea from this work, reflecting a key difference from rigid body grasping, is to specify finger movements rather than grasping forces. Another idea is to obtain the constraints needed for finite element method (FEM)-based deformation updates from tracking the finger-object contacts in an event-based manner. We can sequence the entire operation of picking up a 3D object into periods within each of which the contact configuration does not change under a finite element discretization. During a single period, the displacements of all the contact nodes can be determined. They are used to compute the object's deformation during the period and predict its transition to the next period. All the above require us to first extend the finite element analysis of displacement-based deformation in Jia et al. (2014) from 2D to 3D.

Grasping deformable 3D objects differs from the 2D version of the task in several aspects beyond just the addition of one dimension. Gravity can no longer be ignored given the volume of a 3D object. First, it affects the object's deformation even in the absence of any other external load. Second, gravity needs to be eventually balanced by the finger forces alone in order to lift the object off the supporting plane. Third, gravity is mainly responsible for causing contact slips between the object and the fingertips during a lift. In this paper, we will show how gravity can be factored out of the constitutive equation (which describes deformation) by subtracting from the applied load the initial load on the object exerted by the plane only.

Contact modeling in 3D becomes much more complex and computationally expensive because inside a contact region every FEM node could slide in a continuum of directions (unlike in just one of two opposite directions in the 2D case). We will employ a powerful root finding technique, the homotopy continuation method, to track the sliding nodes.

The object is successfully picked up if no fingertip slips on it during the entire operation. In the FEM

framework, a fingertip slips if and only if all of its nodes in contact with the object slip. To make up for the missing tactile information, a liftability test is performed repeatedly. The test estimates the 'maximum liftable weight', under the current contact configuration, by virtually removing the supporting plane and predicting sliding nodes on the two fingertips. The test outcomes will guide the fingers to either continue squeezing or switch to lifting the object. This pickup strategy will be demonstrated with a Barrett hand successfully over some everyday objects.

Why soft objects generally seem easier to grasp than hard ones? We will examine this issue empirically by comparing the 'efforts' of picking up soft objects and their rigid (and hypothetical) counterparts with the same geometry, density, and contact properties. For fairness of comparison, the initial finger placements on the soft and rigid objects within each pair will also be kept the same. We will characterize the 'effort' as the total normal force exerted by the grasping fingers, excluding tangential forces which are due to friction (and thus passive).

1.1 Paper Outline

The paper studies how to effectively pick up a deformable 3D object resting on a horizontal plane with two robotic fingers. The following mild assumptions are made:

1. The object is deformable and isotropic with uniform mass density.
2. It rests on a horizontal supporting plane.
3. Deformation is small enough to be described under linear elasticity.
4. The two fingertips and the supporting plane are rigid and in frictional contact with the object.
5. Actions are quasi-static.

The last assumption excludes dynamic forces from our consideration such that the finger forces need only balance the object's gravity to pick it up.

Section 2 will review linear elasticity in 3D and the FEM. It will then describe how to deal with the effect of gravity on the object's deformation over a mesh of its resting shape. Afterward, the section will extend the authors' recent result (Jia et al. 2014) on contact-based deformation from 2D to 3D, paving the way for a pickup algorithm to be described in Section 3. In the algorithm, two fingertips squeeze the object until they "feel" it to be liftable without contact sensing. The two components of this algorithm, contact configuration update and liftability test, will be detailed in Sections 4 and 5, respectively. Contact slips will be computed from solving a system of quadratic equations using the homotopy continuation method. We will demonstrate how numerical instability can be avoided via tracking a hypothetical 'liftable weight' as the squeeze proceeds.

Section 6 will present some results from an experiment with a Barrett Hand on picking up five everyday objects. In Section 7, we will perform an empirical comparison with picking up their rigid counterparts with identical shapes and weights, respectively, to reveal why softer objects are generally easier to grasp. This section will also include a couple of examples where a rigid body grasping strategy would fail on soft objects. Some discussion along with several future research directions will be addressed in Section 8.

1.2 Related Work

For literature on rigid body grasping, we refer to the survey by Bicchi and Kumar (2000). To constrain a deformable object from any rigid body movement, the initial finger placement would have to ensure force

closure (Nguyen, 1988) on a rigid body assuming the object's resting shape exactly. It was shown by Salisbury and Roth (1983) that force closure is achieved if and only if the contact wrenches positively span the entire wrench space.

Testing of force closure in 3D with point contacts has been studied for objects with special geometry such as polyhedra (Ponce et al., 1993), for three fingers via geometric reasoning (Li et al. 2003), and for n fingers through linear programming (Trinkle, 1992; Liu, 1999) or by studying the equilibrium of an ordinary differential equation (Bicchi, 1995). In the work by Han et al. (2000), friction cone constraints and mechanical feasibility constraints of the hand were cast into quadratic inequalities in an effort to reduce force closure testing to convex programming that is solvable in polynomial time using the interior point method (Boyd et al., 1994; Nesterov and Nemirovsky, 1994).

The purpose of grasping is for manipulation or transfer. Trinkle and Paul (1989) studied frictionless lifting of a 2D object off its supporting line with two fingers by squeezing it, based on a quasi-static analysis of force and torque equilibria, and on a check for liftability over the object's partitioned boundary.

Investigation on deformable body grasping has not been quite active largely because of rising geometric and mechanical complexities with deformation under grasping forces. Several approaches including bounded force closure (Wakamatsu et al., 1996) and deformation-space closure (Gopalakrishnan and Goldberg, 2005) were proposed for grasping soft 2D objects with limited applicability. Other works were on shape and/or force modeling (Cui and Xiao, 2008; Tian and Jia, 2010), or motion control (Hirai et al., 2001) of already grasped deformable objects.

A comprehensive study was recently conducted by Jia et al. (2014) on grasping general 2D objects with segment contacts under friction. The work introduced displacement-based squeezing, event-based tracking of contact configuration, and several energy-based optimality criteria. The first two of these ideas will be borrowed and extended to 3D in this paper.

Within the FEM framework, the problem of elastic contact with friction had iterative solutions (Sachdeva and Ramakrishnan, 1981; Chandrasekaran et al., 1987), which relied on updating the contact zone and the modes of individual nodes. Our handling of contact takes as input contact displacements for deformation update rather than loads under some imposed constraints (as in the aforementioned works) that are not always realizable.

1.3 Notation

Bold face letters always represent vectors, with the lower case ones denoting points or three-dimensional vectors, and the upper case ones denoting vectors of higher dimensions that aggregate points or three-dimensional vectors. Matrices are represented by non-bold capital letters, and sets of integers (or indices) by letters in the blackboard bold font (e.g. $\mathbb{I}$).

A vector with a caret (e.g. $\hat{\boldsymbol{v}}$) is a unit vector. A vector with a bar (e.g. $\bar{\boldsymbol{v}}$) is formed by some entries from the vector without (e.g. $\boldsymbol{v}$). A node in the FEM representation of an object is referred to as $\boldsymbol{p}_i$, for $1 \leq i \leq n$. When appearing in an expression, $\boldsymbol{p}_i$ also refers to the node's location before deformation, and $\tilde{\boldsymbol{p}}_i$ refers to its location after deformation under the displacement $\boldsymbol{\delta}_i = \tilde{\boldsymbol{p}}_i - \boldsymbol{p}_i$.

All units will be from the metric system. Particularly, we will use meters for length, seconds for time, kilograms for mass, Newtons for force and weight, Pascal for pressure, and Joules for work and energy. These units will be omitted from now on.

2 Deformed Shape under Contact

In this section we will look at how to determine an object's deformation under a squeeze by two fingers, given the displacements of the object's contact points (with the fingers and the supporting plane). How to update the set of contact points and obtain their displacements during the squeeze will be deferred to Section 4. The result from this section will lay the ground for a pickup algorithm to be presented in Section 3.

The section will begin with a brief review of linear elasticity in 3D (Section 2.1), and the FEM formulation of deformation under external loads including gravity (Section 2.2). Then we will show that the effect of gravity can be handled via discounting the support force distribution over the plane contact when the object is at rest (Section 2.3). We will make use of the null space of the object's stiffness matrix and its spectral decomposition (Section 2.4) in the solution of deformation from contact displacements (Section 2.5). By modifying the solution, we will be able to tie up a loose end to compute the plane's support force distribution in the object's resting configuration (Section 2.6).

2.1 Linear Elasticity

Denote the object as $\mathcal{B}$ and consider it under the following displacement field:

$$\boldsymbol{\delta} = (u(x,y,z), v(x,y,z), w(x,y,z))^T,$$

which moves every point $(x,y,z)^T$ to $(x+u, y+v, z+w)^T$. Denote by $\epsilon_x, \epsilon_y, \epsilon_z$ the normal strains along the x-, y-, and z-directions, respectively, and $\gamma_{xy}, \gamma_{xz}, \gamma_{yz}$ the shear strains in the xy-, xz-, and yz-planes, respectively. These strains are expressed as follows:

$$\begin{aligned}
\epsilon_x &= \frac{\partial u}{\partial x}, \\
\epsilon_y &= \frac{\partial v}{\partial y}, \\
\epsilon_z &= \frac{\partial w}{\partial z}, \\
\gamma_{xy} &= \frac{\partial v}{\partial x} + \frac{\partial u}{\partial y}, \\
\gamma_{xz} &= \frac{\partial u}{\partial z} + \frac{\partial w}{\partial x}, \\
\gamma_{yz} &= \frac{\partial w}{\partial y} + \frac{\partial v}{\partial z}.
\end{aligned} \tag{1}$$

The object's strain energy (Crandall et al., 1978, p. 302) is given as

$$U = \frac{E}{2(1+\nu)} \int_{\mathcal{B}} \left((\epsilon_x^2 + \epsilon_y^2 + \epsilon_z^2) + \frac{\nu}{1-2\nu}(\epsilon_x + \epsilon_y + \epsilon_z)^2 + \frac{1}{2}(\gamma_{xy}^2 + \gamma_{xz}^2 + \gamma_{yz}^2) \right) dV, \tag{2}$$

where E and ν are Young's modulus and Poisson's ratio of the material, respectively, with $E > 0$ and $-1 < \nu < \frac{1}{2}$. Most materials (including those considered in this paper) have Poisson's ratio between 0 and $\frac{1}{2}$.

The displacement field $\boldsymbol{\delta}$ is generated under some external force field with density $\boldsymbol{f}(x,y)$ at every point (x,y) inside or on the boundary of the object. The total force potential is $W = -\int_{\mathcal{B}} \boldsymbol{\delta}(x,y)^T \boldsymbol{f}(x,y)\, dV$. The principle of minimum potential energy states that $\boldsymbol{\delta}$ must minimize the total potential energy $\Pi = U + W$ of the system.

2.2 The Finite Element Method

The strain energy (2) generally has no closed form and is evaluated via discretization. Applying the FEM technique (Gallagher, 1975), we discretize the object into a tetrahedral mesh $\mathcal{T}$ with n vertices (or nodes) $\boldsymbol{p}_1, \ldots, \boldsymbol{p}_n$, where $\boldsymbol{p}_i = (x_i, y_i, z_i)^T$, for $1 \leq i \leq n$. Every tetrahedron in the mesh is referred to as an *element*. Figure 2 shows a tomato and its tetrahedral mesh.

(a) (b)

Figure 2: (a) Tomato. (b) Its mesh model consisting of 490 vertices and 2129 tetrahedra.

An external force $\boldsymbol{f}_i$ is applied at each node $\boldsymbol{p}_i$, $1 \leq i \leq n$. Under these forces $\boldsymbol{F} = (\boldsymbol{f}_1^T, \ldots, \boldsymbol{f}_n^T)^T$, the vertex $\boldsymbol{p}_i$ is displaced by $\boldsymbol{\delta}_i$ to the location $\tilde{\boldsymbol{p}}_i = \boldsymbol{p}_i + \boldsymbol{\delta}_i$. Inside each tetrahedron, the displacement of a point is linearly interpolated over those of the four vertices. Thus, the deformed shape is completely described by $\boldsymbol{\Delta} = (\boldsymbol{\delta}_1^T, \ldots, \boldsymbol{\delta}_n^T)^T$, referred to as the *displacement vector*.

The strain energy of an element can be derived based on (2) as a quadratic form in the displacements of its four vertices. Assembled over all tetrahedra in the mesh, the total strain energy takes the form $U = \frac{1}{2}\boldsymbol{\Delta}^T K \boldsymbol{\Delta}$, where K is the $3n \times 3n$ *stiffness matrix*. This matrix is symmetric following Betti's law[1], and positive semidefinite since $U \geq 0$.

We charge the mass of every element evenly to its four vertices. Let m_i be the total mass charged to a vertex $\boldsymbol{p}_i$, $1 \leq i \leq n$. The total gravitational force exerted on $\boldsymbol{p}_i$ thus sums up a quarter of the gravitational force on each tetrahedron it is incident on. Let us write all the nodal gravitation forces into a vector $\boldsymbol{G}$, referred to as the *gravity vector*.

The potential energy of the system is

$$\Pi = \frac{1}{2}\boldsymbol{\Delta}^T K \boldsymbol{\Delta} - \boldsymbol{\Delta}^T (\boldsymbol{F} + \boldsymbol{G}).$$

At equilibrium, it is minimized, leading to the constitutive equation:

$$K\boldsymbol{\Delta} = \boldsymbol{F} + \boldsymbol{G}. \tag{3}$$

Due to the singularity of $\boldsymbol{\Delta}$, boundary conditions are required for solution of (3). They will come from the displacements of contact nodes as they move with the fingertips or stay on the supporting plane.

[1]Betti's law (Saada, 1993, pp. 447–448) states that the deflection at one point in a given direction caused by a unit load at another point in a second direction equals the deflection at the second point in the second direction if the unit load is applied at the first point in the first direction.

2.3 Factoring Gravity out of Deformable Modeling

Because of the gravity vector $\boldsymbol{G}$ on the right hand side of (3), the stiffness matrix is indeed for the object under zero gravity, when its shape is described by the vector $\boldsymbol{P} = (\boldsymbol{p}_1^T, \ldots, \boldsymbol{p}_n^T)^T$.

Before contacted by the fingers, the object rests on the plane. Suppose that the contact area consists of triangles with vertices $\boldsymbol{p}_{k_1}, \boldsymbol{p}_{k_2}, \ldots, \boldsymbol{p}_{k_l}$. Denote by $\boldsymbol{F}_0$ the vector of forces exerted by the plane $\mathcal{P}$ on all the nodes of the object. These contact forces include the effects of friction. Referred to as the *resting support force vector*, $\boldsymbol{F}_0$ has zero entry at every node not in contact with $\mathcal{P}$.

The displacement $\boldsymbol{\Delta}_g$ under gravity satisfies

$$K\boldsymbol{\Delta}_g = \boldsymbol{G} + \boldsymbol{F}_0. \tag{4}$$

Assume that no sliding happens within the contact area during the deformation caused by gravity. Subsequently, the displacements of the contact nodes $\boldsymbol{\delta}_{k_1}, \ldots, \boldsymbol{\delta}_{k_l}$ are all zero, inducing zero work performed by the contact forces.

The shape $\boldsymbol{P}' = \boldsymbol{P} + \boldsymbol{\Delta}_g$ we observe has already deformed under gravity. The stiffness matrix we construct is not K but K' over $\boldsymbol{P}'$. Once the fingers touch and squeeze the object, they will cause further nodal displacements that are represented by the vector $\boldsymbol{\Delta}_f$. These displacements correspond to what we observe as the "deformation" of the object in reality. The constitutive equation becomes

$$K(\boldsymbol{\Delta}_g + \boldsymbol{\Delta}_f) = \boldsymbol{G} + \boldsymbol{F}, \tag{5}$$

where $\boldsymbol{F}$ aggregates the forces exerted on all the nodes by either the plane or a finger. The total displacement under gravity and the contact forces is thus $\boldsymbol{\Delta} = \boldsymbol{\Delta}_g + \boldsymbol{\Delta}_f$.

Subtraction of (4) from (5) yields

$$K\boldsymbol{\Delta}_f = \boldsymbol{F} - \boldsymbol{F}_0. \tag{6}$$

Computation of deformation caused by the fingers should discount the part of the nodal forces that balanced the gravity of the object when it was resting on the plane.

We may estimate the deformation $\boldsymbol{\Delta}_g$ caused by gravity (and thus restore the zero-gravity shape) using the following fixed-point iteration method. The first iteration starts with the observed resting shape $\boldsymbol{P}'$ to construct a first estimate $K^{(1)}$ of the stiffness matrix under zero gravity. Next, plug $K^{(1)}$ into the constitutive equation (4) to compute the displacement $\boldsymbol{\Delta}_g^{(1)}$ that has "presumably happened" under gravity, and then subtract the result[2] from the resting shape to obtain a "corrected" shape estimate $\boldsymbol{P}^{(1)}$. The second iteration starts with $\boldsymbol{P}^{(1)}$ to construct a new stiffness matrix $K^{(2)}$, and obtains a further shape "correction" through (4), and so on. The procedure stops when the change in the shape estimate is small enough. For details we refer to a manuscript by Guo et al. (2014).

Our simulation shows that the above method achieves convergence on a wide range of materials (including hypothetical ones) with density as high as 10^4 and Young's Modulus as low as 5×10^4. However, unless the object has high mass density and low Young's modulus (i.e. very soft), the influence of gravity is quite small and negligible. Modeling of a soft and heavy object (e.g. an animal organ) with large deformation under gravity is also beyond the scope of linear elasticity that we assume. Additionally, there is a paradox with the above fixed-point method. It uses Young's modulus and Poisson's ratio measured under gravity (and thus are influenced by its effect on deformation already). Measuring the two physical parameters for objects in a zero-gravity field before a grasping task would be clearly impractical.

[2] or, for better convergence, a portion r of it, $0 \leq r \leq 1$, together with a portion $1 - r$ of the displacement estimate at the previous step (if it exists)

For the above reasons and to follow the convention in solid mechanics and FEM, we neglect the effect of gravity on the object's resting shape on the plane. More specifically, we identify $\boldsymbol{\Delta}_f$ with $\boldsymbol{\Delta}$ and K' with K. Equation (6) becomes

$$K\boldsymbol{\Delta} = \boldsymbol{F} - \boldsymbol{F}_0. \tag{7}$$

Note that we cannot neglect $\boldsymbol{F}_0$, since it balances the gravitational force, which is on the same order of the grasping force.

2.4 Stiffness Matrix

Solution of (7) will make use of the null space of the stiffness matrix. To describe it, we need to get back to the displacement field $(u, v, w)^T$ introduced in Section 2.1. When the field represents a Euclidean transformation, no change of the object's shape happens. Consequently, all the six strains are zero everywhere inside the object, yielding zero strain energy. The following theorem characterizes this type of displacements.

Theorem 1 *Under linear elasticity, any displacement field $(u, v, w)^T$ that yields zero strain energy is linearly spanned by the following six fields:*

$$\begin{pmatrix} 1 \\ 0 \\ 0 \end{pmatrix}, \begin{pmatrix} 0 \\ 1 \\ 0 \end{pmatrix}, \begin{pmatrix} 0 \\ 0 \\ 1 \end{pmatrix}, \begin{pmatrix} 0 \\ -z \\ y \end{pmatrix}, \begin{pmatrix} z \\ 0 \\ -x \end{pmatrix}, \begin{pmatrix} -y \\ x \\ 0 \end{pmatrix}.$$

See Appendix A for a proof of the theorem. The first three displacement fields in the theorem represent unit translations in the x-, y-, and z-directions, respectively. The next three fields represent rotations about the x-, y-, and z-axes under linear elasticity, respectively. The six fields together describe all rigid body movements.

Applying Theorem 1 and utilizing the linear interpolation within each element of the mesh, we can infer that K has a null space spanned by the following six $3n$-vectors:

$$\begin{aligned} \boldsymbol{t}_x &= (1, 0, 0, 1, 0, 0, \ldots, 0)^T, \\ \boldsymbol{t}_y &= (0, 1, 0, 0, 1, 0, \ldots, 0)^T, \\ \boldsymbol{t}_z &= (0, 0, 1, 0, 0, 1, \ldots, 1)^T, \\ \boldsymbol{r}_x &= (0, -z_1, y_1, 0, -z_2, y_2, \ldots, y_n)^T, \\ \boldsymbol{r}_y &= (z_1, 0, -x_1, z_2, 0, -x_2, \ldots, -x_n)^T, \\ \boldsymbol{r}_z &= (-y_1, x_1, 0, -y_2, x_2, 0, \ldots, 0)^T. \end{aligned} \tag{8}$$

Proposition 2 *The matrix $W = (\boldsymbol{t}_x, \boldsymbol{t}_y, \boldsymbol{t}_z, \boldsymbol{r}_x, \boldsymbol{r}_y, \boldsymbol{r}_z)$ has rank 6 if and only if the nodes $\boldsymbol{p}_1, \boldsymbol{p}_2, \ldots, \boldsymbol{p}_n$ are not collinear.*

We refer the reader to Appendix B for a proof of the proposition. Since even a tetrahedron has four non-collinear nodes, the above proposition implies that the null space of the stiffness matrix K has the full rank 6.

Due to its symmetry, K is diagonalizable with $3n$ independent eigenvectors. Given its six-dimensional null space, K has $3n-6$ positive eigenvalues $\lambda_1, \ldots, \lambda_{3n-6}$ corresponding to unit eigenvectors $\boldsymbol{v}_1, \ldots, \boldsymbol{v}_{3n-6}$. These vectors are orthogonal to the null space of K. Let $\boldsymbol{v}_{3n-5}, \boldsymbol{v}_{3n-4}, \boldsymbol{v}_{3n-3}$ be the unit vectors respectively normalized over $\boldsymbol{t}_x, \boldsymbol{t}_y, \boldsymbol{t}_z$, which are orthogonal to each other. Let $\boldsymbol{v}_{3n-2}, \boldsymbol{v}_{3n-1}, \boldsymbol{v}_{3n}$ be the

unit vectors orthogonalized from $\boldsymbol{r}_x, \boldsymbol{r}_y, \boldsymbol{r}_z$ along with $\boldsymbol{t}_x, \boldsymbol{t}_y, \boldsymbol{t}_z$ using the Gram-Schmidt procedure (Rice, 1964, pp. 45–48). The matrix has a spectral decomposition (Strang, 1993, p. 273) $K = V\Lambda V^T$, where $V = (\boldsymbol{v}_1, \ldots, \boldsymbol{v}_{3n})$, and $\Lambda = \text{diag}(\lambda_1, \ldots, \lambda_{3n-6}, 0, \ldots, 0)$.

2.5 Deformation from Contact Displacements

Now we are ready to solve (7) for the displacement vector $\boldsymbol{\Delta}$ in terms of the resting support force vector $\boldsymbol{F}_0$. Section 2.6 will use a very similar procedure to determine $\boldsymbol{F}_0$ from (4).

As the object is being squeezed by the two fingertips $\mathcal{F}_1$ and $\mathcal{F}_2$, its contact areas with them and the plane are changing. Consistent with the FEM discretization, we view every node on the object's boundary as representing a small neighborhood region. The set of contact nodes will thus not vary during a very small period of squeeze. In Jia et al. (2014), this approach was used in the contact mode analysis for grasping of deformable 2D objects, and experimentally validated. Figure 3 shows an intermediate configuration during a squeeze of the tomato mesh from Figure 2(b) by two hemispherical fingertips. At the moment, there are

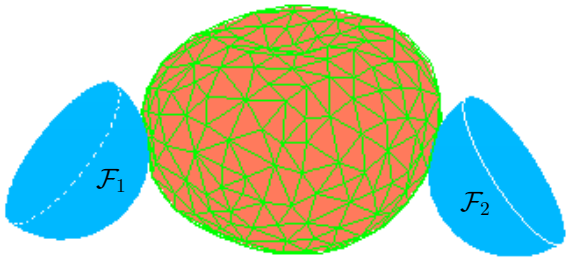

Figure 3: Squeezing the tomato from Figure 2.

seven contact nodes on the plane, three with the left fingertip $\mathcal{F}_1$, and four with the right fingertip $\mathcal{F}_2$.

As in Jia et al. (2014), the starting point of deformable modeling is to compute the object's deformation from specified displacements $\boldsymbol{\delta}_{i_1}, \ldots, \boldsymbol{\delta}_{i_\tau}$ of the τ boundary nodes $\boldsymbol{p}_{i_1}, \ldots, \boldsymbol{p}_{i_\tau}$ that are in contact with either of $\mathcal{F}_1$ and $\mathcal{F}_2$ or the supporting plane. Here we refer to the set $\mathbb{C} = \{i_1, \ldots, i_\tau\}$ as the *contact index set*. The displacement $\boldsymbol{\delta}_{i_1}, \ldots, \boldsymbol{\delta}_{i_\tau}$ are assumed to be small enough that $\mathbb{C}$ does not vary. (Updating of $\mathbb{C}$ will be delayed to Section 4.)

For convenience, let us denote by $\bar{\boldsymbol{a}}$ the vector that selects from a $3n$-vector $\boldsymbol{a}$ the entries indexed at $3i_1 - 2, 3i_1 - 1, 3i_1, \ldots, 3i_\tau - 2, 3i_\tau - 1, 3i_\tau$, which correspond to $\boldsymbol{p}_{i_1}, \ldots, \boldsymbol{p}_{i_\tau}$. For instance, $\bar{\boldsymbol{\Delta}} = (\boldsymbol{\delta}_{i1}^T, \ldots, \boldsymbol{\delta}_{i_\tau}^T)^T$, which is called the *contact displacement vector*.

Given $\bar{\boldsymbol{\Delta}}$, we can solve for the contact force vector[3] $\bar{\boldsymbol{F}}$ and the displacement field $\boldsymbol{\Delta}$ by performing the following procedure similar to the one applied on a planar object in Jia et al. (2014). Substitute the spectral decomposition $K = V\Lambda V^T$ into (7), and left-multiply both sides of the resulting equation with V^T. This yields

$$\begin{aligned} \boldsymbol{v}_k^T\boldsymbol{\Delta} &= \frac{1}{\lambda_k}\boldsymbol{v}_k^T(\boldsymbol{F} - \boldsymbol{F}_0), \quad k = 1, ..., 3n-6, \\ 0 &= \boldsymbol{v}_k^T(\boldsymbol{F} - \boldsymbol{F}_0), \qquad k = 3n-5, \ldots, 3n. \end{aligned}$$

The first group of equations above gives the projections of $\boldsymbol{\Delta}$ onto the first $3n - 6$ eigenvectors. Let the

[3]After factoring out gravity, zero external forces are applied at the non-contact nodes; that is, $\boldsymbol{f}_k = 0$, for $k = 1, \ldots, n$ and $k \notin \mathbb{C}$.

submatrix

$$N = (\boldsymbol{v}_{3n-5}, \ldots, \boldsymbol{v}_{3n}) \tag{9}$$

consist of the last six eigenvectors (which span the null space of the stiffness matrix K), and the vector

$$\boldsymbol{b} = N^T \boldsymbol{\Delta} \tag{10}$$

gather the projections of $\boldsymbol{\Delta}$ onto these eigenvectors. We describe $\boldsymbol{\Delta}$ in terms of all $3n$ eigenvectors:

$$\begin{aligned} \boldsymbol{\Delta} &= \sum_{k=1}^{3n-6} \frac{1}{\lambda_k} (\boldsymbol{v}_k^T (\boldsymbol{F} - \boldsymbol{F}_0)) \boldsymbol{v}_k + N\boldsymbol{b} \\ &= \sum_{k=1}^{3n-6} \frac{1}{\lambda_k} (\bar{\boldsymbol{v}}_k^T \bar{\boldsymbol{F}}) \boldsymbol{v}_k + N\boldsymbol{b} + \boldsymbol{c}, \end{aligned} \tag{11}$$

where

$$\boldsymbol{c} = -\sum_{k=1}^{3n-6} \frac{1}{\lambda_k} (\boldsymbol{v}_k^T \boldsymbol{F}_0) \boldsymbol{v}_k \tag{12}$$

is a constant vector.

Extract the 3τ equations for the displacements $\boldsymbol{\delta}_{i1}, \ldots, \boldsymbol{\delta}_{im}$ of the contact nodes from (11), and combine them with $N^T(\boldsymbol{F} - \boldsymbol{F}_0) = \boldsymbol{0}$, which follows from (7) and $N^T K = 0$. This sets up a linear equation in $\bar{\boldsymbol{F}}$ and $\boldsymbol{b}$:

$$M \begin{pmatrix} \bar{\boldsymbol{F}} \\ \boldsymbol{b} \end{pmatrix} = \begin{pmatrix} \bar{\boldsymbol{\Delta}} - \bar{\boldsymbol{c}} \\ N^T \boldsymbol{F}_0 \end{pmatrix}, \tag{13}$$

where

$$M = \begin{pmatrix} A & B \\ B^T & 0 \end{pmatrix}, \tag{14}$$

with the $3\tau \times 3\tau$ and $3\tau \times 6$ matrices A and B given below:

$$A = \sum_{k=1}^{3n-6} \frac{1}{\lambda_k} \bar{\boldsymbol{v}}_k \bar{\boldsymbol{v}}_k^T, \tag{15}$$

$$B = (\bar{\boldsymbol{v}}_{3n-5}, \ldots, \bar{\boldsymbol{v}}_{3n}). \tag{16}$$

Note that we cannot reduce $N^T \boldsymbol{F}_0$ to $B\bar{\boldsymbol{F}}_0$ because the nodes initially in contact with the plane may no longer be so (and hence not selected by the '$^-$' operator), for instance, when the object is being lifted.

When $\tau = 1, 2$, the six columns of B, each having two or four entries, must be linearly dependent. The singularity of M immediately follows from the linear dependency of its last six rows $(B^T, 0)$ in (14).

By carefully tracing the Gram-Schmidt procedure applied to the six null space vectors in (8), we can show that the vectors $\bar{\boldsymbol{v}}_{3n-6}, \bar{\boldsymbol{v}}_{3n-5}, \ldots, \bar{\boldsymbol{v}}_{3n}$ span the same space as $\bar{\boldsymbol{t}}_x, \bar{\boldsymbol{t}}_y, \bar{\boldsymbol{t}}_z, \bar{\boldsymbol{r}}_x, \bar{\boldsymbol{r}}_y, \bar{\boldsymbol{r}}_z$. Then the statement below about rank of B easily follows from Proposition 2.

Corollary 3 $\mathrm{rank}(B) = 6$ *if and only if there exists at least three non-collinear contacts.*

Theorem 4 *The matrix M defined in (14) is non-singular if and only if the m contact points are not collinear.*

Proof (Necessity) Suppose that the τ contacts are collinear. By Corollary 3, $\mathrm{rank}(B) < 6$. The singularity of M follows directly from its form (14).

(Sufficiency) Suppose that the τ contacts are not collinear. Hence $\tau \geq 3$. It suffices to show that the product $M(\bar{\boldsymbol{F}}^T, \boldsymbol{b}^T)^T \neq \mathbf{0}$ whenever $\bar{\boldsymbol{F}} \neq \mathbf{0}$ or $\boldsymbol{b} \neq \mathbf{0}$. The reasoning is similar to that in Jia et al. (2014) for the 2D case. We first consider the case $\bar{\boldsymbol{F}} = \mathbf{0}$ but $\boldsymbol{b} \neq \mathbf{0}$. The product contains $B\boldsymbol{b}$, which is not zero since the six column vectors of B, ranked 6 under Corollary 3, are linearly independent.

Move on to the other case $\bar{\boldsymbol{F}} \neq \mathbf{0}$. If $B^T\bar{\boldsymbol{F}} \neq \mathbf{0}$, then $M(\bar{\boldsymbol{F}}^T, \boldsymbol{b}^T)^T \neq \mathbf{0}$ trivially from (14). We focus on $B^T\bar{\boldsymbol{F}} = \mathbf{0}$. The rows in the matrix $\bar{V} = (\bar{\boldsymbol{v}}_1, \ldots, \bar{\boldsymbol{v}}_{3n})$ are also of V and thus orthogonal to each other. Hence, $\mathrm{rank}(\bar{V}) = 3\tau$. That $B^T\bar{\boldsymbol{F}} = 0$ then implies that $\bar{\boldsymbol{F}}$ must be a linear combination of $\bar{\boldsymbol{v}}_1, \ldots, \bar{\boldsymbol{v}}_{3n-6}$. We derive

$$\begin{aligned} \bar{\boldsymbol{F}}^T A \bar{\boldsymbol{F}} &= \sum_{k=1}^{3n-6} \frac{1}{\lambda_k} \left(\bar{\boldsymbol{v}}_k^T \bar{\boldsymbol{F}}\right)^2 \\ &> 0, \end{aligned}$$

since there must exist some l, $1 \leq l \leq 3n-6$ such that $\bar{\boldsymbol{v}}_k^T \bar{\boldsymbol{F}} \neq 0$. Subsequently,

$$(\bar{\boldsymbol{F}}^T, \boldsymbol{b}^T) M \begin{pmatrix} \bar{\boldsymbol{F}} \\ \boldsymbol{b} \end{pmatrix} = \bar{\boldsymbol{F}}^T A \bar{\boldsymbol{F}} > 0.$$

□

Under the above theorem, when the contacts are not collinear, the system (13) has a unique solution in terms of $\boldsymbol{F}_0$. Left-multiply both sides of the system with the inverse of M:

$$M^{-1} = \begin{pmatrix} C & E \\ E^T & H \end{pmatrix}, \tag{17}$$

where C, E, and H are matrices of dimensions $3\tau \times 3\tau$, $3\tau \times 6$, and 6×6, respectively. This yields

$$\bar{\boldsymbol{F}} = C(\bar{\boldsymbol{\Delta}} - \bar{\boldsymbol{c}}) + EN^T\boldsymbol{F}_0, \tag{18}$$

$$\boldsymbol{b} = E^T(\bar{\boldsymbol{\Delta}} - \bar{\boldsymbol{c}}) + HN^T\boldsymbol{F}_0. \tag{19}$$

We refer to C as the *reduced stiffness matrix* (Jia et al., 2014) since it relates the contact forces to the specified contact displacements. With both $\bar{\boldsymbol{F}}$ and $\boldsymbol{b}$ determined, the displacement vector follows from (11).

Since $\boldsymbol{c}$ in (12) is linear in terms of the resting support force vector $\boldsymbol{F}_0$, so are $\bar{\boldsymbol{F}}$ in (18) and $\boldsymbol{b}$ in (19). The displacement vector $\boldsymbol{\Delta}$ is thus linear in terms of $\boldsymbol{F}_0$ (and completed determined by it). In Section 2.6 we will discuss how to compute $\boldsymbol{F}_0$.

Before moving on, we can simplify $N^T\boldsymbol{F}_0$. Since $\mathrm{col}(N) = \mathrm{null}(K)$, we left-multiply both sides of (4) with N^T, obtaining

$$\mathbf{0} = N^T\boldsymbol{G} + N^T\boldsymbol{F}_0. \tag{20}$$

Recall that the columns of N are from orthogonalizing the six vectors in (8). It is clear that $\boldsymbol{G}$ is orthogonal to $\boldsymbol{t}_x, \boldsymbol{t}_y$, and $\boldsymbol{r}_z$. By placing the origin at $\frac{1}{m}\sum_{i=1}^n m_i\boldsymbol{p}_i$, where $m = \sum_{i=1}^n m_i$ is the object's mass, we make $\boldsymbol{G}$ orthogonal to $\boldsymbol{r}_x$ and $\boldsymbol{r}_y$ as well. The vector $\boldsymbol{G}$ has a dot product $-w_0$ with $\boldsymbol{t}_z$, where w_0 is the weight of (i.e. the magnitude of the gravitational force on) the object. Hence we obtain

$$N^T\boldsymbol{G} = (0, 0, -w_0/\sqrt{n}, 0, 0, 0)^T, \tag{21}$$

and subsequently by (20),

$$N^T \boldsymbol{F}_0 = (0, 0, w_0/\sqrt{n}, 0, 0, 0)^T.$$

Equations (18) and (19) are simplified to

$$\bar{\boldsymbol{F}} = C(\bar{\boldsymbol{\Delta}} - \bar{\boldsymbol{c}}) + \frac{w_0}{\sqrt{n}} \boldsymbol{e}_3, \tag{22}$$

$$\boldsymbol{b} = E^T(\bar{\boldsymbol{\Delta}} - \bar{\boldsymbol{c}}) + \frac{w_0}{\sqrt{n}} \boldsymbol{h}_3, \tag{23}$$

where $\boldsymbol{e}_3$ and $\boldsymbol{h}_3$ are the third columns of E and H, respectively. Note that $\boldsymbol{c}$ in (12) and $\bar{\boldsymbol{c}}$ in (18) and (19) still depend on $\boldsymbol{F}_0$.

Let us now analyze the time complexities of computing the displacement vector $\boldsymbol{\Delta}$ (and thus the deformed shape) and the contact force vector $\bar{\boldsymbol{F}}$. The spectral decomposition $V \Lambda V^T$ of the stiffness matrix K is computed via singular value decomposition (SVD) in time $O(n^3)$. The component matrices A and B of M are constructed according to (15) and (16) in times $O(\tau^2 n)$ and $O(\tau)$, respectively. The inverse M^{-1} takes additional $O(\tau^3)$ time using, say, Lower Upper (LU) decomposition (Press et al. 2002, pp. 46–50). In time $O(\tau^2 n)$, M and M^{-1} are computed since $n \gg \tau$.

The vector $\bar{\boldsymbol{c}}$ is constructed from (12) by evaluating the entries of $\boldsymbol{c}$ with indices from $\mathbb{C}$ only. Section 2.6 will show that the initial support force vector $\boldsymbol{F}_0$ takes $O(n)$ time to compute, assuming a small number of contacts nodes with the plane when the object is at rest. Every evaluation of the product $\boldsymbol{v}_k^T \boldsymbol{F}_0$ takes $O(1)$ time for the same reason. Hence $\bar{\boldsymbol{c}}$ can be evaluated in $O(\tau n)$ time, and $\boldsymbol{c}$ in $O(n^2)$ time. We obtain $\bar{\boldsymbol{F}}$ and $\boldsymbol{b}$ from (22) and (23) in additional $O(\tau^2)$ and $O(\tau)$ times, respectively. The displacement vector $\boldsymbol{\Delta}$ is then evaluated according to (11) in $O(n^2)$ time.

In summary, given the spectral decomposition of K, in time $O(\tau^2 n + n^2)$ we can update the deformed shape, and in time $O(\tau^2 n)$ we can compute the contact forces. Typically, $\tau \ll n$. Often τ can be treated as a constant. This simplifies the time complexity for deformation update to $O(n^2)$.

2.6 Support Force Vector at Rest

Now we look back at how to determine the vector $\boldsymbol{F}_0$ from (4). We will need to deal with $\boldsymbol{\Delta}_g$ only for this purpose. The procedure is very similar to the one just described in Section 2.5 for specified table and finger contact displacements. The contact index set $\mathbb{C}_0 = \{k_1, \ldots, k_l\}$ refers to all the nodes that are on the supporting plane when the object was at rest. They are known from the mesh construction. Denote by M_0, C_0, E_0 respectively the matrices M, C, E constructed in Section 2.5 under $\mathbb{C}_0$.

We represent the displacement vector $\boldsymbol{\Delta}_g$ under gravity in terms of its projections onto the unit eigenvectors $\boldsymbol{v}_1, \ldots, \boldsymbol{v}_{3n}$ just like in (11):

$$\boldsymbol{\Delta}_g = \sum_{k=1}^{3n-6} \frac{1}{\lambda_k} (\bar{\boldsymbol{v}}_k^T \bar{\boldsymbol{F}}_0) \boldsymbol{v}_k + N \boldsymbol{b}_0 + \boldsymbol{g}, \tag{24}$$

where $\boldsymbol{b}_0$ gathers the projections of $\boldsymbol{\Delta}_g$ onto $\boldsymbol{v}_{3n-5}, \ldots, \boldsymbol{v}_{3n}$, and

$$\boldsymbol{g} = \sum_{k=1}^{3n-6} \frac{1}{\lambda_k} (\boldsymbol{v}_k^T \boldsymbol{G}) \boldsymbol{v}_k. \tag{25}$$

The bar operator '$^-$' now selects entries from a vector with indices from $\mathbb{C}_0$. We end up with a matrix equation similar to (13):

$$M_0 \begin{pmatrix} \bar{\boldsymbol{F}}_0 \\ \boldsymbol{b}_0 \end{pmatrix} = \begin{pmatrix} \bar{\boldsymbol{\Delta}}_g - \bar{\boldsymbol{g}} \\ -N^T \boldsymbol{G} \end{pmatrix} = \begin{pmatrix} -\bar{\boldsymbol{g}} \\ (0, 0, w_0/\sqrt{n}, 0, 0, 0)^T \end{pmatrix}. \tag{26}$$

The last equation above follows from (21) and $\bar{\boldsymbol{\Delta}}_g = \boldsymbol{0}$ since all the contacts nodes with the plane are assumed to be sticking with the plane. Multiply both sides of (26) with M_0^{-1} given in (17):

$$\bar{\boldsymbol{F}}_0 = -C_0 \bar{\boldsymbol{g}} + \frac{w_0}{\sqrt{n}} \boldsymbol{e}_{03}, \tag{27}$$

where $\boldsymbol{e}_{03}$ is the third column of E_0.

The $(3l + 6) \times (3l + 6)$ matrix M_0 is constructed in $O(l^2 n)$ time, and its inverse M_0^{-1} in $O(l^3)$ time to obtain the submatrices C_0 and E_0 of dimensions $3l \times 3l$ and $3l \times 6$, respectively. Afterward, the vector $\bar{\boldsymbol{F}}_0$ is computed using (27) in $O(l^2)$ time. Hence, the overall time spent on computing $\bar{\boldsymbol{F}}_0$ is $O(l^2 n)$, which reduces to $O(n)$ since the number l of initial contact nodes with the plane is very small.

3 The Pickup Algorithm

With deformation computable from specified displacements of the contact nodes, we are now ready to consider how to pick up the object. It is resting on the plane $\mathcal{P}$ with contact nodes $\boldsymbol{p}_k$, $k \in \mathbb{K}_0$. The fingertips $\mathcal{F}_1$ and $\mathcal{F}_2$ make initial point contacts with the object at the nodes $\boldsymbol{p}_i$ and $\boldsymbol{p}_j$, respectively. For both clarity and convenience, we consider $\mathcal{F}_1$ and $\mathcal{F}_2$ to be identically hemispherical. Under Assumption 5 on quasi-static actions, the forces exerted by the fingertips need only balance the object's gravity to lift it up. The strategy is described in Algorithm 1.

3.1 Force Closure Test

Line 1 of Algorithm 1 checks if the finger contact points $\boldsymbol{p}_i$, $\boldsymbol{p}_j$, and the table contact region R would achieve force closure on a rigid body assuming the same shape of the resting object. When the object is squeezed by the fingers, this condition will restrain it from any rigid body movement such that it can only deform. If no force closure under the finger placement, the object will not be fully constrained. The algorithm returns failure.

To our knowledge, computational testing of 3D force closure via area contacts with no approximation has not been investigated. To avoid the complication of dealing with a contact force field over R, we only check if the mesh vertices inside R, that is, $\boldsymbol{p}_k$, $k \in \mathbb{K}_0$, would achieve force closure with $\boldsymbol{p}_i$ and $\boldsymbol{p}_j$. This means that the origin of the wrench space must lie in the interior of the convex hull of primitive unit contact wrenches at these vertices. We apply the algorithm by Liu (1999) to test force closure over the contact set $\{\boldsymbol{p}_k \mid k \in \{i, j\} \cup \mathbb{K}_0\}$. This algorithm shoots a ray from an interior point of the wrench hull toward the origin, and checks if the ray will reach the origin before it exits the hull. Linearizing the contact friction cones as convex polyhedral cones, the algorithm uses linear programming to find the intersection with the hull based on the latter's duality to a convex polytope. The time for the test is $O(s|\mathbb{K}_0|)$ following Liu's analysis, where s is number of sides of the polyhedra cone used to approximate the friction cone.

Algorithm 1 Two-finger pickup of a 3D solid

Input: values of physical parameters, shape geometry, contacts $\mathbb{K}_0 \cup \{i, j\}$, squeeze $(\hat{\boldsymbol{d}}_1, s\hat{\boldsymbol{d}}_2)$
Output: liftoff outcome

1: **if** $\boldsymbol{p}_i$ and $\boldsymbol{p}_j$ are not force closure with the plane contact **then**
2: **return** failure
3: **end if**
4: **while** not yet "liftable" or not enough squeeze **do**
5: increment the squeeze depth ρ
6: update the contact configuration
(Subroutine 2 in Section 4)
7: **if** a fingertip slips **then**
8: **return** failure
9: **end if**
10: update the liftable weight $w(\rho)$
(Subroutine 3 in Section 5)
11: **end while**
12: **if** $w(\rho) \geq w_0$ **then**
13: lift the object off $\mathcal{P}$
14: **if** a fingertip slips **then**
15: **return** failure
16: **else**
17: **return** success
18: **end if**
19: **else**
20: **return** failure
21: **end if**

3.2 Squeeze

After passing the force closure test, the fingertips squeeze the object by translating in constant directions, denoted by unit vectors $\hat{\boldsymbol{d}}_1$ and $\hat{\boldsymbol{d}}_2$, respectively. For every unit distance $\mathcal{F}_1$ translates in $\hat{\boldsymbol{d}}_1$, $\mathcal{F}_2$ translates in $\hat{\boldsymbol{d}}_2$ by $s \geq 0$.[4] The squeeze action is thus represented by $\rho(\hat{\boldsymbol{d}}_1, s\hat{\boldsymbol{d}}_2)$, where ρ, referred to as the *squeeze depth*, is increasing from zero.

The **while** loop of lines 4–11 performs the squeeze until enough upward forces, whether normal or frictional, exist to pick up the object. As the squeeze depth ρ increases, the finger contacts will grow from $\boldsymbol{p}_i$ and $\boldsymbol{p}_j$ into regions. The contact region R with the plane will also change.[5]

The movements of all the sliding nodes are tracked. Their indices form a set $\mathbb{P}$. The indices of all the sticking nodes also form a set $\mathbb{T}$. Together they make up the contact index set $\mathbb{C} = \mathbb{P} \cup \mathbb{T}$. Denote by $\mathbb{I}, \mathbb{J}, \mathbb{K}$ the sets of the indices of the object's surface nodes that are in contact with $\mathcal{F}_1, \mathcal{F}_2, \mathcal{P}$, respectively. They also change as the squeeze continues. Clearly, $\mathbb{C} = \mathbb{I} \cup \mathbb{J} \cup \mathbb{K}$. The *contact state* is characterized by the five index sets $\mathbb{I}, \mathbb{J}, \mathbb{K}, \mathbb{P}, \mathbb{T}$.

We extend the three-finger squeeze-grasp algorithm (involving an adversary finger) from our recent work

[4] If $s = 0$, $\mathcal{F}_2$ is not moving.

[5] Here it is consistent with the FEM to assume that a triangular element is either in contact everywhere or at one of its edges, or not in contact at all.

(Jia et al. 2014) on grasping deformable 2D objects. The squeeze depth ρ will be sequenced such that at every depth in the sequence some event happens to trigger a change in the contact state.

The squeeze continues until the object becomes "liftable", or the amount of squeeze becomes too large that a pickup is deemed impossible under the initial finger placement and the squeezing directions. In the former case, the fingers translate upward to lift the objects. If during the squeeze or pickup all the contacts with one finger are sliding, then the finger slips and the operation fails. This situation is checked on lines 7–9 and 14–15. Otherwise, the object is successfully picked up.

Line 5 of Algorithm 1 applies an extra squeeze in the current iteration. Line 6 updates on the nodes that are in contact with either fingertip or the plane. It also determines whether they are sticking or sliding, and if the latter, how far they will slide. This update will be described in Section 4. After the extra of squeeze, virtual lifting is performed to determine whether the fingers have made enough contact with the object to pick it up. The test, carried out on line 10, will be described in Section 5.

4 Updating Shape and Contact Configuration

Just like in 2D deformable grasping (Jia et al. 2014), during the squeeze the following four events may happen between the object, the supporting plane $\mathcal{P}$, and the two fingertips $\mathcal{F}_1$ and $\mathcal{F}_2$: contact establishment (A), contact break (B), stick-to-slip (C), and slip-to-stick (D). Event A is detected when a node is about to penetrate into $\mathcal{F}_1$, $\mathcal{F}_2$, or $\mathcal{P}$. Event B happens when the contact force at a node is pointing out of the object. Event C takes place when the contact force at a node is going out of its friction cone. Event D occurs when the change rate of the sliding distance of a node with respect to ρ becomes zero.[6]

In this and the next section, we will focus on understanding the extra squeeze applied on the object by the fingertips in one iteration of the **while** loop of lines 4–11 in Algorithm 1. This squeeze is a result of an increase in the squeeze depth ρ from, say, $\rho^{(l)}$, to $\rho^{(l+1)}$ in line 5. This section describes how line 6 updates the contact configuration, which includes the contact state and the locations of all contacts. From now on, we will use a prime to denote the change in a physical quantity due to the extra squeeze (assuming no change in the contact state before it ends). For example, $\bar{\boldsymbol{F}}'$ and $\boldsymbol{\Delta}'$ respectively represent the change in the contact force vector and the displacement vector that have happened under the extra squeeze. It follows from (22) that

$$\bar{\boldsymbol{F}}' = C\bar{\boldsymbol{\Delta}}'. \tag{28}$$

4.1 Extra Displacement of a Node

Subroutine 2 details line 6 in Algorithm 1. It describes the contact configuration update in two rounds. Line 1 of the subroutine evaluates $\bar{\boldsymbol{F}}'$ and $\boldsymbol{\Delta}'$ that would happen with the squeeze depth increment if the contact state does not change.

Every sticking node $\boldsymbol{p}_k$ is assumed to remain sticking during this extra squeeze; namely, its additional displacement is

$$\boldsymbol{\delta}'_k = \mathbf{0}. \tag{29}$$

A node $\boldsymbol{p}_k$ that was sliding at $\rho^{(l)}$ before the extra squeeze is assumed to continue sliding in the same direction. Suppose that it was sliding on the supporting plane in the direction given by the polar angle α_k.

[6]The asymmetry of the conditions for Events C and D is due to contact modeling. Before a sticking contact starts to slip, the contact force is updated by assuming no change in the contact location. A test for Event C is thus based on the rotation of the contact force. Before a sliding contact slows down to stick, the contact movement is updated by assuming the contact force to stay on the friction cone. A test for Event D is thus based on the contact velocity.

Subroutine 2 Contact and deformation update

Input: $\boldsymbol{\Delta}, \mathbb{I}, \mathbb{J}, \mathbb{K}, \mathbb{T}, \mathbb{P}$ at $\rho^{(l)}$
Output: their values at $\rho^{(l+1)}$

1: solve for $\bar{\boldsymbol{F}}'$ and $\boldsymbol{\Delta}'$ based on the contact state just before the extra squeeze in line 5 of Algorithm 1
2: **if** a contact event happens **then**
3: update the index sets $\mathbb{I}, \mathbb{J}, \mathbb{K}$ of finger contacts
4: update the index sets $\mathbb{T}$ and $\mathbb{P}$ of sticking and sliding contacts
5: **end if**
6: solve for contact slips and modify $\bar{\boldsymbol{F}}'$ and $\boldsymbol{\Delta}'$ again based on updated contact state

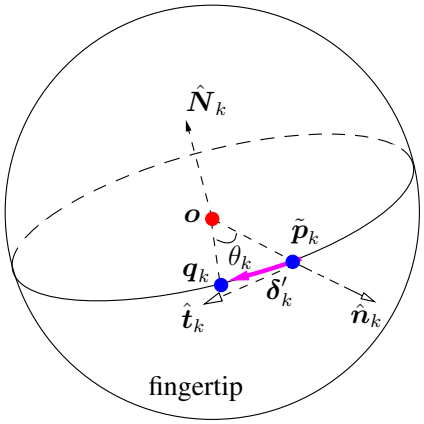

Figure 4: Sliding of a node on a hemispherical fingertip (with the entire sphere shown for clarity of illustration).

The extra displacement of the node over $[\rho^{(l)}, \rho^{(l+1)}]$ is then

$$\boldsymbol{\delta}'_k = d_k(\cos\alpha_k, \sin\alpha_k, 0)^T, \tag{30}$$

where d_k is the sliding distance. That its contact force $\boldsymbol{f}_k$ lies on the boundary of the friction cone is described by the following quadratic equation:

$$(1+\mu_{\mathcal{P}}^2)(\boldsymbol{f}_k \cdot \hat{\boldsymbol{z}})^2 = \boldsymbol{f}_k \cdot \boldsymbol{f}_k, \tag{31}$$

where $\mu_{\mathcal{P}}$ is the coefficient of contact friction between the object and the plane.

The situation that a node $\boldsymbol{p}_k$ slides on a fingertip is illustrated in Figure 4. At $\rho^{(l)}$, $\boldsymbol{p}_k$ was at the position $\tilde{\boldsymbol{p}}_k$ with the normal $\hat{\boldsymbol{n}}_k$ pointing out of the fingertip. Let $\hat{\boldsymbol{t}}_k$ be the tangential direction in which it was sliding at the moment. We assert that the node $\boldsymbol{p}_k$ will reach some point $\boldsymbol{q}_k$ on the great circle co-planar with $\hat{\boldsymbol{t}}_k$ and $\hat{\boldsymbol{n}}_k$. The change in the displacement as a result of this extra squeeze will be

$$\boldsymbol{\delta}'_k = \boldsymbol{q}_k - \tilde{\boldsymbol{p}}_k. \tag{32}$$

The unit normal $\hat{\boldsymbol{N}}_k$ to the plane containing this great circle is in the direction of $\hat{\boldsymbol{t}}_k \times \hat{\boldsymbol{n}}_k$. Essentially, $\boldsymbol{q}_k$ is obtained from rotating $\tilde{\boldsymbol{p}}_k$ about $\hat{\boldsymbol{N}}_k$ through some angle $\theta_k < 0$. We have $\boldsymbol{q}_k = \boldsymbol{o} + c_k(\tilde{\boldsymbol{p}}_k - \boldsymbol{o}) + s_k(\hat{\boldsymbol{N}}_k \times (\tilde{\boldsymbol{p}}_k - \boldsymbol{o}))$, where $\boldsymbol{o}$ is the center of the fingertip, and c_k and s_k are the shorthand notations for $\cos\theta_k$ and $\sin\theta_k$, respectively. Under Coulomb's law, the force $\boldsymbol{f}_k$ is on the friction cone. This induces a quadratic equation:

$$(1+\mu_{\mathcal{F}}^2)(\boldsymbol{f}_k \cdot \hat{\boldsymbol{n}}_k)^2 = \boldsymbol{f}_k \cdot \boldsymbol{f}_k, \tag{33}$$

coupled with

$$c_k^2 + s_k^2 = 1. \tag{34}$$

In the above, $\mu_{\mathcal{F}}$ is the coefficient of friction between the object and the fingertip.

4.2 Contact Configuration after the Extra Squeeze

The extra displacement of a contact node $\boldsymbol{p}_k$ is summarized below over (29), (30), and (32):

$$\boldsymbol{\delta}'_k = \begin{cases} \mathbf{0} & \text{if } k \in \mathbb{T}, \\ d_k(\cos\alpha_k, \sin\alpha_k, 0)^T & \text{if } k \in \mathbb{P} \cap \mathbb{K}, \\ \boldsymbol{q}_k - \tilde{\boldsymbol{p}}_k & \text{if } k \in \mathbb{P} \cap (\mathbb{I} \cup \mathbb{J}). \end{cases} \tag{35}$$

The change $\bar{\boldsymbol{\Delta}}'$ in the contact displacement vector is in terms of d_k, $k \in \mathbb{P} \cap \mathbb{K}$, and $c_l = \cos\theta_l$, $s_l = \sin\theta_l$, $l \in \mathbb{P} \cap (\mathbb{I} \cup \mathbb{J})$. So is $\bar{\boldsymbol{F}}'$ given in (28). Add $\bar{\boldsymbol{F}}'$ to the value $\bar{\boldsymbol{F}}^{(l)}$ of $\bar{\boldsymbol{F}}$ before the extra squeeze, and plug the result into (31), or (33) and (34). We end up with a system of quadratic equations in the same number of variables:

$$\begin{aligned} (1+\mu_{\mathcal{P}}^2)(\boldsymbol{f}_k \cdot \hat{\boldsymbol{z}})^2 &= \boldsymbol{f}_k \cdot \boldsymbol{f}_k, \quad k \in \mathbb{P} \cap \mathbb{K}; \\ (1+\mu_{\mathcal{F}}^2)(\boldsymbol{f}_l \cdot \hat{\boldsymbol{n}}_l)^2 &= \boldsymbol{f}_l \cdot \boldsymbol{f}_l, \quad l \in \mathbb{P} \cap (\mathbb{I} \cup \mathbb{J}), \\ c_l^2 + s_l^2 &= 1, \quad l \in \mathbb{P} \cap (\mathbb{I} \cup \mathbb{J}). \end{aligned} \tag{36}$$

Solve the above system using the homotopy continuation method (Garcia and Zangwill, 1979; Allgower and Georg, 1997) for d_k, $k \in \mathbb{P} \cap \mathbb{K}$, and c_l, s_l, $l \in \mathbb{P} \cap (\mathbb{I} \cup \mathbb{J})$. Details on the solution are offered in Appendix C.

We determine the change $\boldsymbol{\Delta}'$ in the shape using (11) and (23):

$$\boldsymbol{\Delta}' = \sum_{k=1}^{3n-6} \frac{1}{\lambda_k}(\bar{\boldsymbol{v}}_k^T \bar{\boldsymbol{F}}')\boldsymbol{v}_k + (\boldsymbol{v}_{3n-5}, \ldots, \boldsymbol{v}_{3n})E^T \bar{\boldsymbol{\Delta}}', \tag{37}$$

where the change $\bar{\boldsymbol{F}}'$ in the contact force is given in (28). Assign $\boldsymbol{\Delta} \leftarrow \boldsymbol{\Delta}^{(l)} + \boldsymbol{\Delta}'$ and $\bar{\boldsymbol{F}} \leftarrow \bar{\boldsymbol{F}}^{(l)} + \bar{\boldsymbol{F}}'$.

Based on the updated $\boldsymbol{\Delta}$ and $\bar{\boldsymbol{F}}$, line 2 of Subroutine 2 checks for contact events. If an event happens, lines 3 and 4 then update the contact index sets $\mathbb{I}, \mathbb{J}, \mathbb{K}, \mathbb{T}, \mathbb{P}$.

With the matrix C already computed in line 1, the expression of $\bar{\boldsymbol{F}}'$ in terms of d_ks, c_ls, and s_ls can be obtained in $O(\tau^2)$ time, where τ is the number of contact nodes. The system (36) is set up in extra $O(\tau^2)$ time. The running time of the homotopy continuation method will be derived in Appendix C to be $O(\tau^3 r)$, where r is the size of discretization of the interval $[0, 1]$ used by the method.

4.3 Recomputing Contact Slips

With the updated contact state after the extra squeeze, we go back to re-estimate how much the sliding nodes have moved during the period of the extra squeeze, and subsequently, recompute $\boldsymbol{\Delta}'$ and $\bar{\boldsymbol{F}}'$. A second round of computation thus takes place in line 6 of Subroutine 2. First, we determine the (new) sliding direction of each node $\boldsymbol{p}_k$, $k \in \mathbb{P}$. Then its sliding distance can be described by either d_k or θ_k (i.e. c_k and s_k) depending on whether sliding happens on the supporting plane or a fingertip.

Figure 5 shows a node $\boldsymbol{p}_k$ that has been determined to have switched from sticking to sliding during the extra squeeze. Its contact force $\boldsymbol{f}_k$ computed in line 1 is out of the friction cone; namely, $(1+\mu_{\mathcal{P}}^2)(\boldsymbol{f}_k \cdot \hat{\boldsymbol{z}})^2 <$

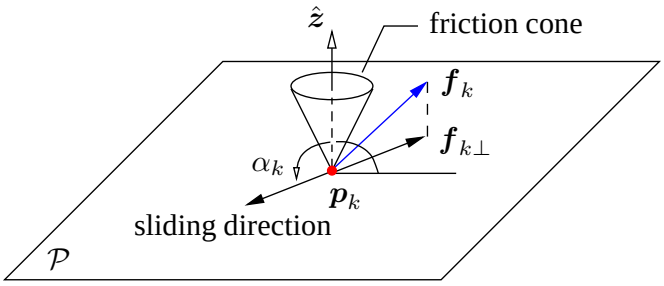

Figure 5: Sliding of a node on the supporting plane.

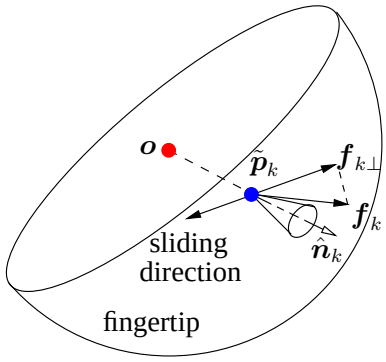

Figure 6: Sliding direction of a node on the fingertip.

$\|\boldsymbol{f}_k\|^2$. Project $\boldsymbol{f}_k$ onto $\mathcal{P}$ to obtain $\boldsymbol{f}_{k\perp} = \boldsymbol{f} - (\boldsymbol{f} \cdot \hat{\boldsymbol{z}})\hat{\boldsymbol{z}}$. The sliding direction, represented by the polar angle α_k, is the opposite of $\boldsymbol{f}_{k\perp}$.

Suppose a node $\boldsymbol{p}_k$ in contact with a fingertip is determined to have switched from sticking to sliding. The contact force $\boldsymbol{f}_k$, out of the friction cone at its position $\tilde{\boldsymbol{p}}_k$, has a tangential component $\boldsymbol{f}_{k\perp} = \boldsymbol{f}_k - (\boldsymbol{f}_k \cdot \hat{\boldsymbol{n}}_k)\hat{\boldsymbol{n}}_k$. We assert that the node $\boldsymbol{p}_k$ will be sliding in the direction opposite to that of $\boldsymbol{f}_{k\perp}$ during this extra squeeze. This is illustrated in Figure 6.

Computing the increments $\bar{\boldsymbol{F}}$ and $\bar{\boldsymbol{\Delta}}$ in line 1 of Subroutine 2 is as expensive as computing $\bar{\boldsymbol{F}}$ and $\boldsymbol{\Delta}$. Based on the analysis from Section 3, they take $O(n^2)$ time, where n is the number of nodes. This cost also dominates the combined time cost of contact event detection in line 2 and contact index set updates in lines 3–4. The computation of contact slips and the updates in the increments of the contact force and displacement vectors takes $O(\tau^3 r)$ time, where τ is the number of contact nodes and r is the number of discretized intervals over $[0, 1]$ used by the homotopy continuation method. The subroutine takes a total of $O(n^2 + \tau^3 r)$ time, and so does line 6 in Algorithm 1.

It is important to model nodal sliding despite the computational cost. Otherwise, errors in the locations of the contact nodes could accumulate over all the incremental steps to yield a false prediction by the liftability test to be introduced in the next section. This could lead to failure of the physical operation. A more detailed explanation along with some error analysis is given in Appendix D.

5 Liftability Test

When the squeeze depth ρ is small, the contact regions on the fingertips are small and unable to create enough friction to hold the object if it is to be picked up. As ρ increases, the fingertips $\mathcal{F}_1$ and $\mathcal{F}_2$ may stop squeezing at the moment they "feel" that the object is liftable. To check on such "feeling", line 10 of Algorithm 1 conducts a virtual liftability test repeatedly as ρ increases. Such a test, involving no physical action, predicts the finger contact forces at the current ρ value if the supporting plane $\mathcal{P}$ were to be removed, and then checks if one of $\mathcal{F}_1$ and $\mathcal{F}_2$ would end up slipping as a result. A fingertip slip is indicated by either $\mathbb{I} \cap \mathbb{P} = \mathbb{I}$ or $\mathbb{J} \cap \mathbb{P} = \mathbb{J}$, where $\mathbb{I}, \mathbb{J}, \mathbb{P}$ are the index sets of the nodes in contact with $\mathcal{F}_1$, $\mathcal{F}_2$, and sliding, respectively.

A straightforward liftability test might be performed in the following manner. We let the set $\mathbb{C}$ of contact nodes suddenly reduce from $\mathbb{I} \cup \mathbb{J} \cup \mathbb{K}$, where $\mathbb{K}$ includes the indices of the nodes in contact with the plane $\mathcal{P}$, to $\mathbb{I} \cup \mathbb{J}$ as if the supporting plane $\mathcal{P}$ were removed. Then, we recompute the contact force vector in two rounds as in Subroutine 2, handling nodal slips if any. If $\mathcal{F}_1$ or $\mathcal{F}_2$ slips, the squeeze test fails and the object is not liftable at the current squeeze depth.

The issue with the above binary test is numerical convergence. The movements of the sliding nodes are solved from the system (36) of quadratic equations, in a manner sensitive to the initial guess. Dramatic reduction in the contact set $\mathbb{C}$ from $\mathbb{I} \cup \mathbb{J} \cup \mathbb{K}$ to $\mathbb{I} \cup \mathbb{J}$ causes a big change to the system such that the finger contact positions in the configuration $\mathbb{I} \cup \mathbb{J} \cup \mathbb{K}$ would serve as a very bad initial guess in the contact configuration $\mathbb{I} \cup \mathbb{J}$. Such change is too dramatic for tracking the contact positions even using the homotopy continuation method.

We would like to find a quantity that directly reflects the continual progress made by the two fingers towards lifting the object up. Its value should change with the squeeze depth ρ, and can be updated incrementally just like the contact configuration.

This leads us to the notion of 'liftable weight'. Imagine the object's weight to be unknown. At zero squeeze depth, $\mathcal{F}_1$ and $\mathcal{F}_2$ exert zero contact force. The object would be liftable only if it had zero weight. At a squeeze depth ρ, the *liftable weight* $w(\rho)$ is the maximum (hypothetical) weight of the object that would not result in any fingertip sliding if $\mathcal{P}$ were removed. The harder the two fingertips squeeze, the more weight they tend to be able to lift. Physics will ensure the function w to be continuous in ρ. Generally, we expect w to be also monotonically increasing.

The idea is then to track $w(\rho)$ as ρ increases until it equals the real weight w_0 of the object. Consider the lth iteration of the **while** loop of lines 4–11 in Algorithm 1, when the squeeze depth increases from, say, $\rho^{(l)}$ to $\rho^{(l+1)}$. Line 10 expands into Subroutine 3, which obtains $w(\rho^{(l+1)})$ based on the contact configuration at $\rho^{(l+1)}$ and the liftable weight $w(\rho^{(l)})$ at $\rho^{(l)}$. It iterates to test the weights $w(\rho^{(l)}) + h$, $w(\rho^{(l)}) + 2h$, ..., for some small increment h, until the object is no longer liftable at some $w(\rho^{(l)} + kh)$, $k > 0$. Then, set $w(\rho^{(l+1)}) = w(\rho^{(l)}) + (k-1)h$.

Line 1 in the subroutine saves the shape and contact configuration at the newly increased squeeze depth $\rho^{(l+1)}$. They result from the extra squeeze performed in line 5 of Algorithm 1, and are updated in line 6 (i.e. by Subroutine 2).

In line 3 of Subroutine 3, the contact index set is set to $\mathbb{I} \cup \mathbb{J}$, to reflect the hypothetical removal of the supporting plane. The **while** loop of lines 4–10 determines the liftable weight at the squeeze depth $\rho^{(l+1)}$ by performing a virtual lift operation as follows. Line 6 recomputes the (hypothetical) finger contact forces $\bar{\boldsymbol{F}}$ according to (22) with w_0 replaced by w. Lines 7–8 detect the contact events and, if any, update the contact state accordingly. Line 9 checks if one of the fingertip slips.

After line 11 updates the liftable weight over the new squeeze depth $\rho^{(l+1)}$, the saved (real) shape and

Subroutine 3 Update of Liftable Weight

Input: Liftable weight $w(\rho^{(l)})$
Output: Liftable weight $w(\rho^{(l+1)})$

1: save $\boldsymbol{\Delta}$, $\mathbb{I}, \mathbb{J}, \mathbb{K}, \mathbb{T}, \mathbb{P}$, $\boldsymbol{c}$
2: $w \leftarrow w(\rho^{(l)})$
3: $\mathbb{C} \leftarrow \mathbb{I} \cup \mathbb{J}$
4: **while** no finger slips **do**
5: $\quad w \leftarrow w + h$
6: $\quad$ re-evaluate $\bar{\boldsymbol{F}}$ according to (22) with w_0 replaced by w
7: $\quad$ detect contact events
8: $\quad$ update $\mathbb{I}, \mathbb{J}, \mathbb{T}, \mathbb{P}$
9: $\quad$ determine if $\mathbb{I} \cap \mathbb{P} = \mathbb{I}$ or $\mathbb{J} \cap \mathbb{P} = \mathbb{J}$
10: **end while**
11: $w(\rho^{(l+1)}) \leftarrow w - h$
12: restore $\boldsymbol{\Delta}$, $\mathbb{I}$, $\mathbb{J}$, $\mathbb{K}$, $\mathbb{T}$, $\mathbb{P}$, $\boldsymbol{c}$

contact configurations are restored. The execution goes back to line 4 of Algorithm 1.

Since the squeeze depth ρ undergoes a small increment, small changes occur to the contact configuration and the liftable weight $w(\rho)$. This makes tracking of w feasible. Once w reaches or exceeds the actual weight w_0 of the object, the liftability test is passed[7].

Figure 7 shows the tomato from Figure 2 grasped by two hemispherical plastic fingertips of radius 0.2 mounted on the fingers of a Barrett Hand. As plotted in (a), the ratio w/w_0 increases monotonically with the squeeze depth ρ. The object becomes liftable (i.e. $w/w_0 = 1$) when $\rho = 0.0176$. The moment is shown in (b) with seven contact nodes on each finger and five in the plane. The object is lifted off the plane (shown in (c)) immediately afterward.

Let us analyze the running time of a single iteration of the **while** loop of lines 4–10 in Subroutine 3. Line 6 takes $O(\tau^2 n)$ times for τ contact nodes, as analyzed in Section 2.5, respectively. Lines 7–9 take time on the order of the number of surface nodes, which is $O(n^{2/3})$ for a uniform tetrahedral mesh. Thus, one iteration of the **while** loop takes $O(\tau^2 n)$ time.

Finally, it is time to analyze the running time of Algorithm 1. Let ρ^* be the squeeze depth at which the liftability test is passed, and d the increment in ρ in line 5 of the algorithm. There are a total of ρ^*/d such increments. Each increment leads to a call of Subroutine 2, which takes $O(n^2 + \tau^3 r)$ time based on the analysis in Section 4. Meanwhile, there are a total of w_0/h increments in the liftable weight w starting from 0. Note that w_0/h counts the iterations of the **while** loop of lines 4–10 in Subroutine 3 over all the calls to the subroutine by Algorithm 1. Every such iteration takes time $O(\tau^2 n)$, as we just analyzed. Combining the two types of costs, we have that Algorithm 1 takes $O((\rho^*/d)(n^2 + \tau^3 r) + (w_0/h)\tau^2 n)$ time. Note that $w_0/h \gg \rho^*/d$ because every call to Subroutine 3 increments w multiple times.

Once the liftability test is passed, in line 13 of Algorithm 1 the two fingers translate upward. During the lift, the nodal contacts with the plane $\mathcal{P}$ will break one by one, and some contacts with the fingertips could also break under the gravitational force. Contact modeling, however, is no different from that in squeezing. If a fingertip slips during the lift, the pickup fails. Otherwise, the pickup is a success once the object breaks contact with the plane.

[7] To be conservative, we may continue increasing ρ until $w(\rho)$ exceeds the object's original weight by a certain margin.

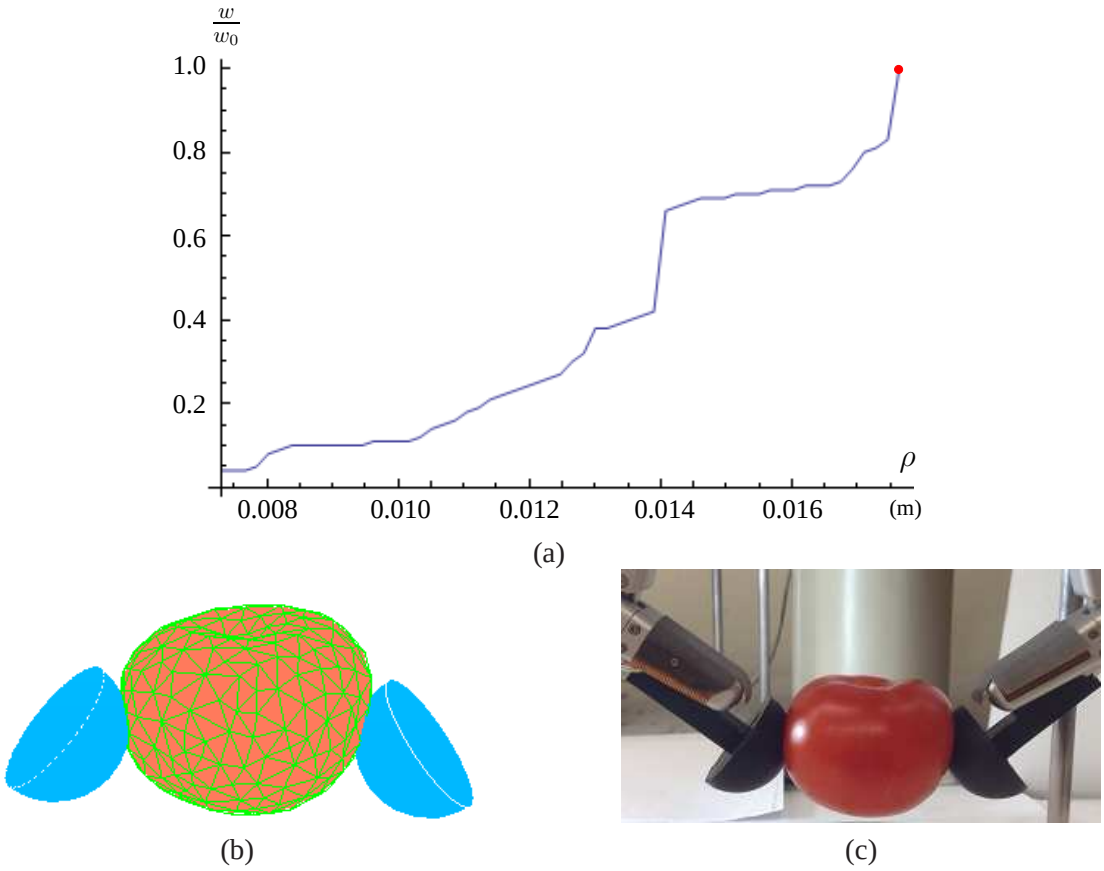

Figure 7: Liftability test for the tomato in Figure 2. (a) Ratio of the liftable weight w to the tomato's actual weight $w_0 = 1.246$ increases with the squeeze depth ρ. (b) Shape and contact configuration at the squeeze depth $\rho = 0.0088$ when the tomato becomes liftable. (c) Liftoff of the tomato at the same squeeze depth. Young's modulus $E = 10^5$, Poisson's ratio $\nu = 0.4$, and the coefficient of friction $\mu_{\mathcal{F}} = 0.32$ for the finger-tomato contacts.

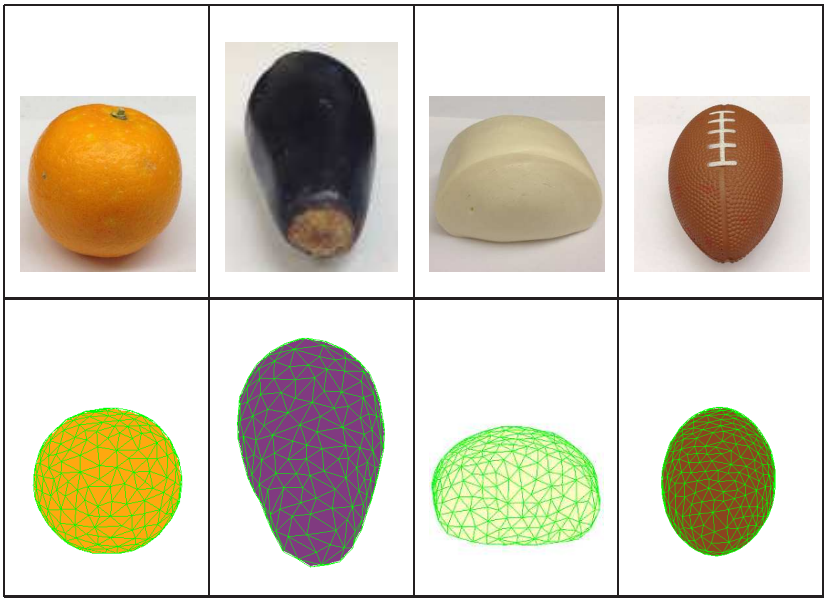

Table 1: Objects (a) at rest and (b) in tetrahedral mesh representations.

6 Experiment

Experiment was performed with a 3-fingered Barrett Hand mounted with hemispherical fingertips of radius 0.02. These fingertips are made of the material acetal. Tetrahedral meshes for objects used in the experiment were first acquired by a 3D scanner from Next Engine, Inc., and then simplified using MeshLab[8]. Generation of tetrahedral meshes and transformation of the objects were implemented using the Computational Geometry Algorithm Library (`http://www.cgal.org`). All computation was performed on a PC with an Intel Core i7-3770 Processor and 8 GB system RAM.

To validate Algorithm 1, we experimented over the tomato in Figure 2, and four other objects in Table 1: an orange, an eggplant, a steamed bun, and a toy football. Table 2 lists the mesh and physical parameter values of all five deformable objects. In the table, $\mu_{\mathcal{P}}$ and $\mu_{\mathcal{F}}$ are the coefficients of friction between the plane and the object and between the fingertips and the object, respectively.[9]

The result on the tomato was already shown in Figure 7. On all five objects, the two fingertips applied a squeeze $\rho(\hat{\boldsymbol{d}}_1, \hat{\boldsymbol{d}}_2)$, where $\hat{\boldsymbol{d}}_1 = (0, 0.974, -0.227)$ and $\hat{\boldsymbol{d}}_2 = (0, -0.974, -0.227)$. As soon as the liftability test was passed at the squeeze depth ρ^*, the fingers switched their action from squeezing to lifting.

In Table 3, the first row shows the four objects picked up by the Barrett Hand, the second row shows the simulation results, at the squeeze depths listed in the third row, respectively. The fourth row lists the numbers of contact nodes when the objects are in the air. The fifth row lists the simulation times (in seconds) of Algorithm 1 before the pickup, which were significantly less than the times spent on computing the spectral decompositions of the stiffness matrices using the SVD, which were 53.7, 99.0, 106.3, 130.6, and 299.2, respectively.

How closely does the liftability test capture the moment when an object becomes liftable? Some comparison is needed between the minimum squeeze passing the liftability test and the minimum squeeze for

[8] `http://meshlab.sourceforge.net/`

[9] A method for measuring E, ν, $\mu_{\mathcal{P}}$, and $\mu_{\mathcal{P}}$ was described in Appendix B in Jia et al. (2014).

	Tomato	Orange	Eggplant	Bun	Football
# Vert.	490	600	612	658	875
# Facets	498	564	616	646	782
# Tetra.	2129	2692	2676	2941	4058
w_0	1.246	1.868	3.336	0.467	0.489
E	1.0×10^5	1.4×10^5	1.1×10^5	2×10^3	6×10^3
ν	0.4	0.4	0.4	0.2	0.3
$\mu_{\mathcal{F}}$	0.32	0.34	0.5	0.4	0.45
$\mu_{\mathcal{P}}$	0.35	0.36	0.6	0.42	0.47

Table 2: Parameters with the objects in Figure 2 and Table 1.

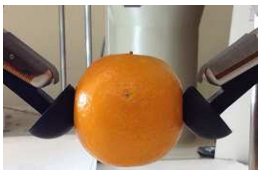			
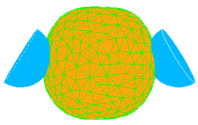	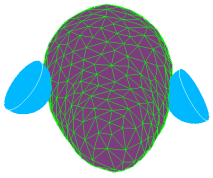	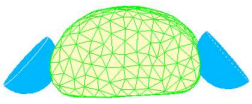	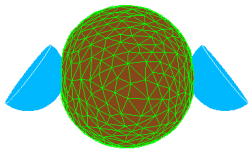
$\rho^* = 0.0124$	0.0071	0.0052	0.0053
# nodes: 15	8	10	8
Simul. time: 2.75	2.41	3.12	2.54

Table 3: Successful pickups of four deformable objects. The liftoff configurations in experiment (row 1) and simulation (row 2). Row 3 lists the squeeze depths passing the liftability test at which the action switches to pickup. Rows 4 and 5 display respectively the numbers of contact nodes at liftoff and the simulation times.

a liftoff. Let f^* be the magnitude of the total squeeze force exerted by the fingers at the squeeze depth ρ^* passing the test. Meanwhile, denote by $\rho_{\min}$ the minimum squeeze depth for a liftoff, and $f_{\min}$ the magnitude of the total force exerted by the two fingers at the moment of the object fully breaking its contact with the table during this liftoff.

For each of the five objects used in the experiment, $\rho_{\min}$ can be computed via bisection over $[0, \rho^*]$, knowing that $\rho = \rho^*$ has resulted in a success and $\rho = 0$ (i.e. no squeeze) will lead to a failure. For every intermediate value of ρ, the corresponding squeeze and the following lift attempt are simulated by updating the shape and contact configuration as described in Section 4. The outcome is a success if no finger slips on the object before the object breaks contact with the table, and a failure otherwise.

Table 4 compares (ρ^*, f^*) with $(\rho_{\min}, f_{\min})$ over the five objects under the same finger placements and squeeze directions in the experiment. We see that for every object ρ^* and f^* are slightly greater than $\rho_{\min}$

	Tomato	Orange	Eggplant	Bun	Football
ρ^*	0.01764	0.0247	0.01412	0.01028	0.01058
f^*	2.173	3.041	3.881	0.727	0.632
$\rho_{\min}$	0.01587	0.02383	0.01355	0.00982	0.01039
$f_{\min}$	2.055	2.913	3.74	0.638	0.605

Table 4: Comparisons between the squeeze depth ρ^* predicted by the liftability test and the minimum squeeze depth $\rho_{\min}$ for lift off, and between the corresponding total forces f^* and $f_{\min}$ exerted by the two fingers. The results are listed for the five objects used in the experiment.

and $f_{\min}$, respectively. This suggests that the liftability test is conservative. This can be explained as follows. In the liftability test the supporting plane is suddenly removed, while in calculating $\rho_{\min}$ the object breaks contact with the table one node after another. In the latter scenario, less force needs to be exerted on the object to keep the fingertips from sliding, and subsequently, less squeeze needs to be performed.

We also performed an experiment to determine the minimum squeeze to pick up the football. With repeated attempts by the robot hand in the manner of bisecting the squeeze depth, the value of $\rho_{\min}$ was estimated as 0.01032. The grasping force 0.611 was resolved from the readings of the strain gauges mounted at the finger joints of the Barrett Hand. These values are very close to those obtained from simulation as shown in the last column of Table 4.

7 Comparison with Rigid Body Grasping

Experience tells us that soft objects are often easier to grasp and pick up than hard ones. This section will empirically demonstrate such perception through simulation over synthetic objects with adjustable softness. Then it will show that some rigid body grasping strategies such as antipodal grasping sometimes are not applicable to deformable objects either because their required finger placements cannot be realized or because such a grasp will result in finger sliding due to deformation.

The two fingertips in all simulation instances in this section will have the same geometry as the plastic ones used in the experiment in Section 6.

	Tomato	Orange	Eggplant	Steamed bun	Football
Deform. (a)	2.77	4.54	7.02	1.05	1.00
Deform. (b)	2.68	4.35	6.86	1.01	0.96
Rigid	2.96	4.82	7.41	1.16	1.09

Table 5: Total normal forces exerted by the fingertips during the pickups shown in Figure 7(a) and row 1 of Figure 3: (a) at passing the liftability test and (b) after the pickup. (c) Minimum normal forces to pick up five rigid objects respectively with the shapes and masses of the soft objects and under the same (initial) contact positions.

7.1 Liftoff Effort

We compare the deformable grasping results in Table 3 with those of picking up five synthetic and rigid bodies that respectively assume the same shapes and masses as the tomato, orange, eggplant, bun, and football. The contact locations on such a rigid object are also the same as the initial contact locations on the corresponding deformable object.

The upward translation distances by the fingertips during a successful pickup are irrelevant. Tangential contact forces are due to friction and thus passive. For the above reasons, we measure the *liftoff effort* as the total normal force f_N exerted by the two grasping fingertips. On a deformable body, it is computed as the sum of the normal forces at the contact nodes at two moments: when the liftability test has just been passed and when the object is completely in the air. For a rigid body, we use the *minimal* total normal force. Appendix E shows that this minimization reduces to one with a linear objective function subject to some quadratic constraints, and offers an efficient solution.

Table 5 summarizes the comparison results. The first two rows respectively list the total normal forces to (a) pass the test and (b) keep the objects in the air. A comparison between them shows that when an object is lifted off the plane, the total normal force has reduced slightly. This is because, once the object is in the air, the portion of the normal contact force previously balanced by the plane is no longer needed, and gravity has also caused some change in the shape to comply with the fingertip geometry.

Within every column of the table, the two normal forces to pick up a soft object are less than the minimum normal force to pick up its rigid counterpart, not to mention that these normal forces on the soft object could be considerably larger than the minimum required for a pickup.

The following explanation can be offered for the above comparison result. Under the squeeze, a soft object deforms to have spherical concavities that match the fingertip geometry through contact. These contact areas have regions in which the inward normal always has an upward component. This allows the normal contact forces exerted by the fingertips to play a more direct role in balancing the gravitational force on the object. In the case of a rigid object, such balance is mostly provided by the frictional force. Since the coefficient of friction is often less than one (cf. Table 2), this means less normal contact force needs to be generated by the grasping fingers in the case of a comparable soft object.

7.2 Liftoff Effort Varying with Softness

To illustrate how the liftoff effort varies with softness, we simulate over an object with exactly the same shape and mass as the tomato in Figure 2(a), but varying Young's modulus E and Poisson's ratio ν. The object becomes rigid as $E \to \infty$ and $\nu \to 0$. The same initial contact positions and squeeze directions for the tomato in the experiment in Figure 7 are used.

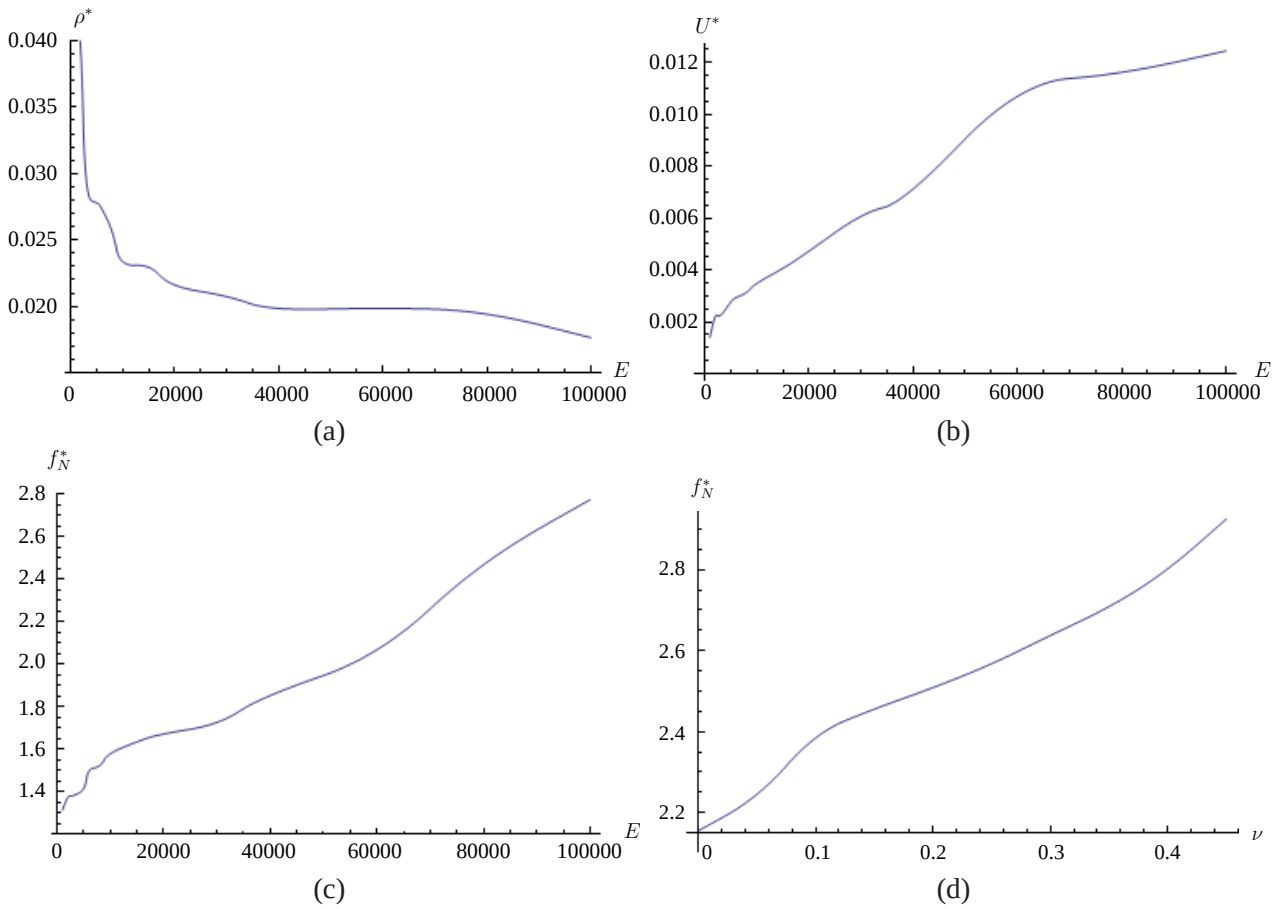

Figure 8: Lifting up objects with tomato's shape and mass but varying values of Young's modulus E and Poisson's ratio ν. As E increases (while $\nu = 0.4$), to pass the liftability test, (a) the required squeeze depth ρ^* decreases, (b) the strain energy U^* increases, and (c) the total normal force f_N^* at this depth increases. (d) The total normal force at ρ^* increases with ν (while $E = 10^5$).

Denote by U^* and f_N^* respectively the strain energy and the total normal force at the squeeze depth ρ^* that passes the liftability test. We plot ρ^*, U^*, and f_N^* against E in the range $[0, 10^5]$ (while keeping $\nu = 0.4$), and f_N^* against ν in the range $[0, 0.49]$[10] (while keeping $E = 10^5$).

Figure 8(a) shows that less squeeze depth is needed to pick up a harder object (i.e. one with a higher E value). Despite the decrease in the squeeze depth, (b) shows that higher strain energy has built up at the moment the liftability test is passed. This implies that more work has been done by the fingers. In (c), when the E value increases, the total normal force at ρ^* to pass the liftability test (and thus to pick up the object) increases. This agrees with our perception that harder objects are more difficult to pick up.

On the other hand, Figure 8(d) interestingly shows that f_N^* increases with Poisson's ratio ν, though the amount is small. Unlike Young's modulus, which describes the relative elongation or compression in the direction of an applied load, Poisson's ratio describes the relative change orthogonal to this direction. The larger the value of ν, the more the object stretches tangentially at a finger contact. The object's shape conforms less to the fingertips locally, resulting in more needed normal contact force.

[10]This is the range of values for most materials.

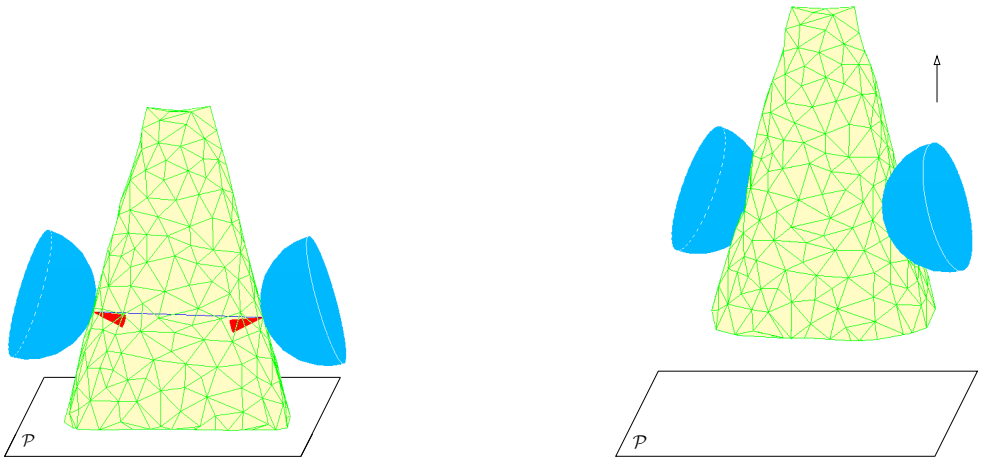

(a) (b)

Figure 9: Soft truncated cone resting on the plane $\mathcal{P}$ under a non-force-closure finger placement in (a) is successfully picked up due to deformation in (b). Also drawn in (a) are the friction cones at the initial contact points and the segment connecting them that lies outside the cones. Physical parameters of the cone: mass 0.06578, $E = 10^5$, $\nu = 0.3$. Geometric parameters: height 0.1, top face radius 0.01, bottom face radius 0.0325. The left and right finger contacts are initially at 0.040456 and 0.040292 above the plane.

7.3 Failure of Rigid Body Grasping Strategies

A rigid body grasping strategy typically exerts pre-computed forces that achieve force and torque equilibria on a rigid object, knowing that the object's shape will not change under these forces. On a deformable object, such a strategy may break either because there is no available finger placement required by the strategy or because such a finger placement cannot be maintained once the object starts to deform.

Let us first consider a truncated cone sitting on the plane $\mathcal{P}$ as shown in Figure 9(a). Given the cone geometry and a coefficient of friction value 0.2, no pair of reachable surface points could form force closure without the plane. This is because the contact friction cone at every reachable point is downward such that the two fingers cannot exert upward forces to balance the object's gravity if it were rigid. A rigid body grasping analysis would find no strategy for picking up the object. However, since the object is deformable, the fingertips start at a non-force-closure placement in (a) successfully lifts the object off the plane as shown in (b), by squeezing it first along the inward normals for 0.004 and then toward each other for 0.002 before the pickup.

In Figure 10, the two fingertips squeezing a U-shaped magnet are about to loose their grip due to the resulting deformation. The fingertips make the initial contacts at a pair of antipodal points, and squeeze toward each other in opposite directions. Both fingertips begin to slip at the squeeze depth 0.007, when there are three contact nodes on each fingertip and five in the plane.

8 Discussion

We have described a simple squeeze-and-lift strategy for two fingers to pick up deformable 3D objects resting on a table, with no use of touch sensing. The action of squeezing is chosen for its simplicity from both analysis and execution points of view. It exploits the constraining nature of a force-closure grasp at the start, and leverages growing contact areas due to deformation to provide the needed amount of friction for a

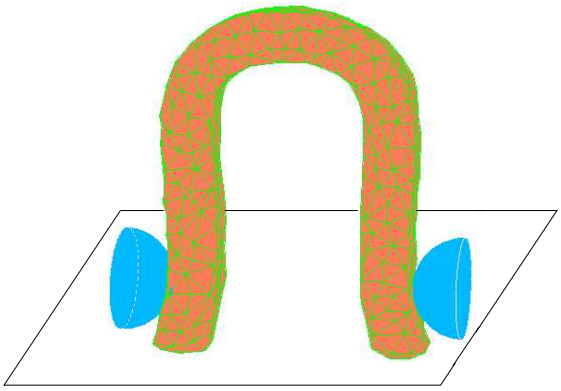

Figure 10: Failure in grasping a U-shaped magnet at two antipodal positions due to insufficient friction to keep the fingertips from sliding as the magnet deforms under their squeeze. Physical parameters of the magnet: mass 0.119129, $E = 10^5$, $\nu = 0.3$; $\mu_{\mathcal{F}} = \mu_{\mathcal{P}} = 0.1$. Geometric parameters: height 0.128, side length of square cross section 0.02, distance between the centers of the two feet 0.106. Initial contact locations are 0.03 above the plane.

pickup.

Under such a squeeze, an object's changing shape and its contact configuration with the fingers are modeled using the FEM in an event-based manner. To support the modeling, we have extended the displacement-based finite element analysis in Jia et al. (2014) to 3D, with a novel treatment of the gravity effect on deformation. Contact slips are estimated via root finding of quadratic systems derived under Coulomb friction and linear elasticity. The necessity for modeling contact slips is supported by a preliminary error analysis given in Appendix D.

During the squeeze, a liftability test is repeatedly conducted to predict when to switch the action to lifting. The test estimates the "liftable portion" of the object's weight for the current amount of squeeze. Squeeze depth stepping shared by both modeling and testing dramatically eases the computation involved in the latter, which boils down to solution of a large quadratic system, by tracking the common roots of a nearby system (i.e. the one just before the squeeze depth increment), in terms of convergence and efficiency. Intuitively, the test emulates the human hand's feeling of a grip on an object that it is trying to pick up.

Experimental results with everyday objects demonstrate the appeal and effectiveness of the grasping strategy in its simple physical execution. We have also examined the reason why deformable objects are easier to grasp than rigid objects via an empirical comparison.

8.1 Practicality

Just like in rigid body grasping, a vision system is needed to guide the initial finger placement. Over the 3D images of an object acquired using two or more cameras[11], a mesh can be constructed instantaneously. The volume is easily computed over the mesh, and the weight is obtained if the density of the material is known. The density can often be looked up, or if not, need only be measured once beforehand for all objects of the same material.

Knowledge of the exact weight is often unnecessary, as long as some upper bound can be estimated[12]. The fingertips may keep squeezing until the "liftable weight" exceeds this upper bound by a certain margin.

[11]The use of multiple cameras eliminates or reduces the occlusion effect.

[12]which is true for many everyday items, for instance, fruits.

The requirement for Young's modulus and Poisson's ratio does not hinder the strategy's applicability, especially in handling multiple objects of the same material. The values of these two parameters can be looked up for many materials. If not, we can measure them easily, for instance, using the method by Jia et al. (2014). The coefficients of sticking and sliding friction can either be looked up or measured easily too.

On the computation side, obtaining the SVD of the stiffness matrix takes $O(n^3)$ time, and each deformation update takes $O(n^2)$ time, where n is the number of nodes in the tetrahedra mesh. In our presented experiment, the SVD is the dominating part which took up to five minutes on the objects, while simulation of the squeeze-and-pick operation took about three seconds, which was comparable to the time of the physical operation. Note that SVD is only a one-time overhead for identical objects. We can cut down the SVD time effectively as follows. Since points in the object's interior are displaced much less than those on its boundary (especially the ones in contact with the fingertips), we can use a mesh that has nodes distributed more sparsely the inner they are. So the total number n of nodes is proportional to the count on the surface, which is currently $O(n^{2/3})$ assuming the uniform distribution of nodes in the mesh generation. Consequently, the simulation time can be cut down by a factor of n. The number of nodes may be further reduced, since we have observed that the grasping outcome does not depend on very high mesh resolution. Exponential growth in the computing power will make the SVD time even less of an issue.

8.2 Extensions

Algorithm 1 can be slightly modified to work with three or more fingertips, because Subroutine 2 on shape and contact configuration updates and Subroutine 3 on the liftability test essentially operate on sets of contact nodes with no discrimination between individual fingers. Non-spherical fingertips will merely affect the computation involved in tracking contact events and estimating contact slips, as the system (36) needs to be expressed in terms of a different set of fingertip parameters to locate contacts.

Failure happens when a fingertip slips on the object. This could be due to a bad initial finger placement, or a poor choice of the squeezing directions. Both are related to the robustness issue. A quick solution would be to first simulate several combinations of initial placements and squeezing directions, and then execute the one that results in the smallest portion of sliding nodes on the fingertips at the moment when the liftability test is passed.

It is important to understand how uncertainties in the physical properties may affect the outcome. One direction is to extend the preliminary error analysis in Appendix D to take into account an interval of possible values for each investigated physical parameter.

To address the failure issue at depth, we need to consider general finger movements—along arbitrary paths—during a squeeze. The example in Figure 9 uses a path consisting of two straight movements. Typically, a continuum of squeeze paths exist for a successful liftoff. If we can assign some measure to every squeeze path, then the problem will be transformed into an optimization. Optimal initial finger placements may also be studied under this framework. We have made some progress on the investigation of planning a squeeze trajectory that yields minimum finger work.

Another aspect of improvement is to turn the strategy into a reactive one by incorporating tactile data for slip detection/prediction, and designing a feedback control loop based on such data. This will make the pickup behavior more closely resemble that of the human hand.

Funding

Support for this research was provided in part by Iowa State University (ISU), and in part by the National Science Foundation through the grant IIS-0915876. Any opinions, findings, and conclusions or recommendations expressed in this material are those of the author(s) and do not necessarily reflect the views of the National Science Foundation.

Acknowledgment

We would like to thank the anonymous reviewers of The International Journal of Robotics Research for their insights and constructive comments. Early results have appeared in a paper (Lin et al. 2014) at the IEEE International Conference on Robotics and Automation. We owe thanks to the anonymous conference reviewers for their thorough reading and valuable feedback. Also, we acknowledge the use of online code from Computational Geometry Algorithm Library (`http://www.cgal.org`).

References

[1] Allgower EL and Georg K (1997) Numerical path following. In Ciarlet PG et al. (eds): *Handbook of Numerical Analysis*, vol. 5, North-Holland.

[2] Bicchi A (1995) On the closure properties of robotic grasping. *The International Journal of Robotics Research* 14(4):319–334.

[3] Bicchi A and Kumar V (2000) Robotic grasping and contact: a review. In: *Proceedings of the IEEE International conference on robotics and automation*, pp. 348–353.

[4] Boyd S, El Ghaoui L, Feron E and Balakrishnan V (1994) *Linear Matrix Inequalities in System and Control Theory*. Philadelphia, PA: SIAM.

[5] Chandrasekaran N, Haisler WE and Goforth RE (1987) A finite element solution method for contact problems with friction. *International Journal of Numerical Methods in Engineering* 24(3):477–495.

[6] Crandall SH, Dahl NC and Lardner TJ (1978) *An Introduction to the Mechanics of Solids*. 2nd edn. New York City, NY: McGraw-Hill.

[7] Cui T and Xiao J (2008) Simulation of grasping deformable objects with a virtual human hand. In: *Proceedings of the IEEE/RSJ International conference on intelligent robots and systems*, pp. 3965–3970.

[8] Gallagher RH (1975) *Finite Element Analysis: Fundamentals*. Englewood Cliffs, NJ: Prentice-Hall.

[9] Garcia CB and Zangwill WI (1979). Finding all solutions to polynomial systems and other systems of equations. *Mathematical Programming* 16:159–176.

[10] Gopalakrishnan K and Goldberg K (2005) D-space and deform closure grasps of deformable parts. *The International Journal of Robotics Research* 24(11):899–910.

[11] Guo F, Wang F, Lin H and Jia YB (2014) Recovering the gravity-free shape and stiffness matrix of a deformable solid for accurate modeling and interaction. `http://www.cs.iastate.edu/~jia/papers/zero-gravity-shape.pdf`. February, 2014.

[12] Han L, Trinkle JC, and Li ZX (2000) Grasp analysis as linear matrix inequality problems. *IEEE Transactions on Robotics and Automation* 16(6):663–674.

[13] Hirai S, Tsuboi T, and Wada T (2001). Robust grasping manipulation of deformable objects. In: *Proceedings of the IEEE Symposium on assembly and task planning*, pp. 411–416.

[14] Jia YB, Guo F, and Lin H (2014) Grasping deformable planar objects: squeeze, stick/slip analysis, and energy-based optimalities. *The International Journal of Robotics Research*, 33(5):866–897.

[15] Li JW, Liu H and Cai HG (2003) On computing three-finger force-closure grasps of 2-D and 3-D objects. *IEEE Transactions on Robotics and Automation* 19(1):155–161.

[16] Lin H, Guo F, Wang F and Jia YB (2014) Picking up soft 3D objects with two fingers. In: *Proceedings of the IEEE International Conference on Robotics and Automation*, pp. 3656–3661.

[17] Liu YH (1999) Qualitative test and force optimization of 3-D frictional form-closure grasps using linear programming. *IEEE Transactions on Robotics and Automation* 15(1):163–173.

[18] Morgan AP (1983) A method for computing all solutions to systems of polynomial equations. *ACM Transactions on Mathematical Software* 9(1):1–17.

[19] Nesterov Y and Nemirovsky A (1994) *Interior-Point Polynomial Methods in Convex Programming*. Philadelphia, PA: SIAM.

[20] Nguyen VD (1988) Constructing force-closure grasps. *The International Journal of Robotics Research* 7(1):3–16.

[21] Ponce J, Sullivan S, Boissonnat JD and Merlet JP (1993) On computing four-finger equilibrium and force-closure grasps of polyhedral objects. *The International Journal of Robotics Research* 16(1):11–35.

[22] Press WH, Teukolsky SA, Vetterling WT, et al. (2002) *Numerical Recipes in C++*, 2nd edn. Cambridge, UK: Cambridge University Press.

[23] Rice JR (1964) *The Approximation of Functions*. Addison-Wesley Publishing Company.

[24] Sachdeva TD and Ramakrishnan CV (1981) A finite element solution for the two-dimensional elastic contact problems with friction. *International Journal of Numerical Methods in Engineering* 17(8):1257–1271.

[25] Sadd MH (2009) *Elasticity: Theory, Applications, and Numerics*. 2nd edn. Waltham, MA: Academic Press.

[26] Saada AS (1993) *Elasticity: Theory and Applications*. Malabar, FL: Krieger Publishing Company.

[27] Salisbury JK and Roth B (1983) Kinematic and force analysis of articulated mechanical hands. *Journal of Mechanisms, Transmissions, and Automation in Design* 105(1):35-41.

[28] Strang G (1993) *Introduction to Linear Algebra*. 2nd edn. Wellesley, MA: Wellesley-Cambridge Press.

[29] Tian J and Jia YB (2010) Modeling deformations of general parametric shells grasped by a robot hand. *IEEE Transactions on Robotics* 26(5):837–852.

[30] Trinkle JC and Paul RC (1989) The initial grasp liftability chart. *IEEE Transactions on Robotics and Automation* 5(1): 47–52.

[31] Trinkle J (1992) A quantitative test for form closure grasps. In: *Proceedings of the IEEE/RSJ International conference on intelligent robots and systems*, pp. 1670–1677.

[32] Wakamatsu H, Hirai S and Iwata K (1996) Static analysis of deformable object grasping based on bounded force closure. In: *Proceedings of the IEEE/RSJ International conference on intelligent robots and systems*, pp. 3324–3329.

A Proof of Theorem 1

Proof (Sufficiency) It is straightforward to check that under any of the six fields all strains vanish:

$$\epsilon_x = \epsilon_y = \epsilon_z = \gamma_{xy} = \gamma_{xz} = \gamma_{yz} = 0. \tag{38}$$

(Necessity) Suppose $U = 0$. First, from (2) we show that (38) must hold. This is clearly true for $0 \leq \nu < \frac{1}{2}$. When $-1 < \nu < 0$, we rewrite the sum of the first two summands in the integrand in (2) as

$$\frac{1+\nu}{1-2\nu}(\epsilon_x^2 + \epsilon_y^2 + \epsilon_z^2) - \frac{\nu}{1-2\nu}\Big((\epsilon_x - \epsilon_y)^2 + (\epsilon_y - \epsilon_z)^2 + (\epsilon_z - \epsilon_x)^2\Big).$$

Since $-1 < \nu < 0$, the coefficients of all square terms in the original integrand are non-negative. Hence, these terms must vanish, implying (38).

From (1), vanishing of the normal strains $\epsilon_x, \epsilon_y, \epsilon_z$ implies

$$u = u(y,z), \quad v = v(x,z), \quad \text{and} \quad w = w(x,y).$$

Vanishing of the shear strain γ_{xy} yields $\partial v/\partial x + \partial u/\partial y = 0$ which, together with the independence of u from x and v from y, implies

$$\frac{\partial u}{\partial y} = -\frac{\partial v}{\partial x} = a(z),$$

for some function a. Similarly, from $\gamma_{xz} = 0$ and $\gamma_{yz} = 0$ we respectively derive

$$\begin{aligned} \frac{\partial w}{\partial x} &= -\frac{\partial u}{\partial z} = b(y), \\ \frac{\partial v}{\partial z} &= -\frac{\partial w}{\partial y} = c(x). \end{aligned}$$

For each of u, v, w, we integrate its two partial derivatives above, and equate the results. This yields

$$u = a(z)\cdot y + \alpha(z) = -b(y)\cdot z + \omega(y), \tag{39}$$
$$v = -a(z)\cdot x + \beta(z) = c(x)\cdot z + \theta(x), \tag{40}$$
$$w = b(y)\cdot x + \gamma(y) = -c(x)\cdot y + \phi(x), \tag{41}$$

for some functions $\alpha, \beta, \gamma, \omega, \theta$, and ϕ.

Consider (39), for instance. The first expression of u is linear in y, while the second one is linear in z. We immediate infer that

$$\begin{aligned} a(z) &= \rho_1 z + \rho_2, && (42)\\ b(y) &= -\rho_1 y + \rho_3, && (43)\\ \alpha(z) &= -\rho_3 z + \rho_4, && (44)\\ \omega(y) &= \rho_2 y + \rho_4, && (45) \end{aligned}$$

for some constants ρ_1, ρ_2, ρ_3, and ρ_4. Carry out similar reasoning over the two expressions of v in (40) to obtain

$$\begin{aligned} c(x) &= -\rho_1 x + \rho_5, && (46)\\ \beta(z) &= \rho_5 z + \rho_6, && (47) \end{aligned}$$

for some ρ_5 and ρ_6, and over those two of w in (41) to obtain

$$\begin{aligned} c(x) &= \rho_1 x + \rho_7, && (48)\\ \gamma(y) &= -\rho_7 y + \rho_8, && (49) \end{aligned}$$

for some ρ_7 and ρ_8. Comparing the two forms (46) and (48), we infer that $\rho_1 = 0$ and $\rho_5 = \rho_7$. That $\rho_1 = 0$ reduces (42), (43), and (48) respectively to

$$a(z) = \rho_2, \quad b(y) = \rho_3, \quad c(x) = \rho_7. \tag{50}$$

Substitute the expressions of $a(z)$ from (50) and $\alpha(z)$ from (44) into the first equation of (39), we obtain

$$u = \rho_2 y - \rho_3 z + \rho_4.$$

Similarly, we plug $a(z)$ from (50) and $\beta(z)$ from (47) into the first equation of (40), and $b(y)$ from (50) and $\gamma(y)$ from (49) into the first equation of (41). This results in

$$\begin{aligned} v &= -\rho_2 x + \rho_5 z + \rho_6,\\ w &= \rho_3 x - \rho_5 y + \rho_8, \end{aligned}$$

where the last equation is after substitution of $\rho_7 = \rho_5$. Thus, we have established that

$$\begin{aligned} \begin{pmatrix} u \\ v \\ w \end{pmatrix} &= -\rho_5 \begin{pmatrix} 0 \\ -z \\ y \end{pmatrix} - \rho_3 \begin{pmatrix} z \\ 0 \\ -x \end{pmatrix} - \rho_2 \begin{pmatrix} -y \\ x \\ 0 \end{pmatrix}\\ &\quad + \rho_4 \begin{pmatrix} 1 \\ 0 \\ 0 \end{pmatrix} + \rho_6 \begin{pmatrix} 0 \\ 1 \\ 0 \end{pmatrix} + \rho_8 \begin{pmatrix} 0 \\ 0 \\ 1 \end{pmatrix}. \end{aligned}$$

□

B Proof of Proposition 2

In this appendix, we show that the rank of $W = (\boldsymbol{t}_x, \boldsymbol{t}_y, \boldsymbol{t}_z, \boldsymbol{r}_x, \boldsymbol{r}_y, \boldsymbol{r}_z)$, with its column vectors given in (8), is six if and only if there are three or more non-collinear contacts. We focus on the case of three non-collinear nodes $\boldsymbol{p}_i, \boldsymbol{p}_j, \boldsymbol{p}_k$, and later show that the case with more than three non-collinear nodes is easy to handle. Let us consider the following 9×6 submatrix of W:

$$Q = (\bar{\boldsymbol{t}}_x, \bar{\boldsymbol{t}}_y, \bar{\boldsymbol{t}}_z, \bar{\boldsymbol{r}}_x, \bar{\boldsymbol{r}}_y, \bar{\boldsymbol{r}}_z). \tag{51}$$

Here the bar operator '$^-$' selects entries corresponding to $\boldsymbol{p}_i, \boldsymbol{p}_j, \boldsymbol{p}_k$.

To determine $\mathrm{rank}(Q)$, for $l = 1, 2, 3$ we subtract row l from rows $l+3$ and $l+6$. This yields

$$Q_1 = \begin{pmatrix} I_3 & P \\ 0 & Q_2 \\ 0 & Q_3 \end{pmatrix},$$

where

$$Q_2 = \begin{pmatrix} 0 & z_j - z_i & y_i - y_j \\ z_i - z_j & 0 & x_j - x_i \\ y_j - y_i & x_i - x_j & 0 \end{pmatrix},$$

$$Q_3 = \begin{pmatrix} 0 & z_k - z_i & y_i - y_k \\ z_i - z_k & 0 & x_k - x_i \\ y_k - y_i & x_i - x_k & 0 \end{pmatrix}.$$

Since $\mathrm{rank}(Q) = \mathrm{rank}(Q_1)$, we will focus on Q_1. Straightforward calculation shows that $\det(Q_2) = 0$. From $\boldsymbol{p}_i \neq \boldsymbol{p}_j$ we have $\mathrm{rank}(Q_2) = 2$.

When $\boldsymbol{p}_i, \boldsymbol{p}_j, \boldsymbol{p}_k$ are collinear, $\boldsymbol{p}_k - \boldsymbol{p}_i = \lambda(\boldsymbol{p}_j - \boldsymbol{p}_i)$ for some λ. This implies $Q_3 = \lambda Q_2$. Therefore, $\mathrm{rank}(Q_1) = 5$, which implies that Q and W all have rank 5. The above argument generalizes to $m > 3$ contacts in that $\mathrm{rank}(W) = 5$ when $\boldsymbol{p}_{i_1}, \ldots, \boldsymbol{p}_{i_\tau}$ are collinear. Geometrically, when all the nodes are collinear, the object is free to rotate about the line through these nodes. This establishes the necessity in Proposition 2.

The sufficiency will follow from the lemma below.

Lemma 5 $\mathrm{rank}(Q) = 6$ *if* $\boldsymbol{p}_i, \boldsymbol{p}_j, \boldsymbol{p}_k$ *are not collinear.*

Proof We see that $\mathrm{rank}(Q) = \mathrm{rank}(Q_1) = 6$ if and only if the rank of $\binom{Q_2}{Q_3}$ is 3. Because $\boldsymbol{p}_i \neq \boldsymbol{p}_j$, without loss of generality, we assume $x_i \neq x_j$. Let $\lambda = (x_k - x_i)/(x_j - x_i)$. In the matrix $\binom{Q_2}{Q_3}$, subtract rows 2 and 3, scaled by λ, from rows 5 and 6, respectively. This yields the following matrix:

$$Q_4 = \begin{pmatrix} 0 & z_j - z_i & y_i - y_j \\ z_i - z_j & 0 & x_j - x_i \\ y_j - y_i & x_i - x_j & 0 \\ 0 & z_k - z_i & y_i - y_k \\ (z_i - z_k) - \lambda(z_i - z_j) & 0 & 0 \\ (y_k - y_i) - \lambda(y_j - y_i) & 0 & 0 \end{pmatrix}.$$

There are two cases:

- $y_k - y_i \neq \lambda(y_j - y_i)$. In column 1 of Q_4, zero all but the last entry by subtracting multiples of the last row from the first five rows. Columns 2 and 3 are not affected. Rows 2, 3, 6 of the resulting matrix, each with only one non-zero element in a different column, are linearly independent.

- $y_k - y_i = \lambda(y_j - y_i)$. Then $z_k - z_i \neq \lambda(z_j - z_i)$ must hold since the three points are not collinear. The last row of Q_4 contains all zeros. Zero all but the fifth entry in column 1 via subtractions of multiples of row 5. Again, columns 2 and 3 are not affected. Rows 2, 3, 5 are linearly independent.

Thus, we have shown the rank of $\binom{Q_2}{Q_3}$ to be 3. □

For $m > 3$ nodes that are not collinear, we can always select three non-collinear nodes, which define a submatrix of Q with rank 6. Hence, $\mathrm{rank}(Q) = 6$. Thus, the non-collinearity of all the nodes is also a sufficient condition.

C Slip Computation using the Homotopy Continuation Method

Recall that the system (36) describes the movements of all sliding contact nodes during an extra squeeze by the fingers. There are $\xi = |\mathbb{P} \cap \mathbb{K}|$ nodes sliding in the plane, and $\eta = |\mathbb{P} \cap (\mathbb{I} \cup \mathbb{J})|$ nodes sliding on either of the two fingertips. In (35), rename the sliding distance variables d_k, $k \in \mathbb{P} \cap \mathbb{K}$, as $u_1, \ldots, u_\xi$; c_k, $k \in \mathbb{P} \cap (\mathbb{I} \cup \mathbb{J})$, as $u_{\xi+1}, \ldots, u_{\xi+\eta}$; and s_k, $k \in \mathbb{P} \cap (\mathbb{I} \cup \mathbb{J})$ as $u_{\xi+\eta+1}, \ldots, u_{\xi+2\eta}$. Let $\zeta = \xi + 2\eta$. Apparently, $\zeta = O(\tau)$ for τ contact nodes.

From (35) the contact displacement vector $\bar{\boldsymbol{\Delta}}$ is linear in $u_1, u_2, \ldots, u_\zeta$. So is the contact force vector $\bar{\boldsymbol{F}}$ by (22), with the force exerted at the kth node represented as

$$\boldsymbol{f}_k = \begin{pmatrix} f_{kx} \\ f_{ky} \\ f_{kz} \end{pmatrix} = \begin{pmatrix} \sum_{i=1}^{\zeta} a_{kxi} u_k + b_{kx} \\ \sum_{i=1}^{\zeta} a_{kyi} u_k + b_{ky} \\ \sum_{i=1}^{\zeta} a_{kzi} u_k + b_{kz} \end{pmatrix}, \tag{52}$$

for some constants $a_{kxi}, a_{kyi}, a_{kzi}$, $1 \leq i \leq \zeta$, and b_{kx}, b_{ky}, b_{kz}.

Given the plane normal $\hat{\boldsymbol{z}} = (0, 0, 1)^T$, the first group of equations in (36) is rewritten as

$$(1 + \mu_{\mathcal{P}}^2)(f_{kz})^2 = f_{kx}^2 + f_{ky}^2 + f_{kz}^2, \tag{53}$$

for $k \in \mathbb{P} \cup \mathbb{K}$. The unit normal $\hat{\boldsymbol{n}}_l = (n_{lx}, n_{ly}, n_{lz})^T$ at the sliding node $\boldsymbol{p}_l$ on a fingertip, $l \in \mathbb{P} \cap (\mathbb{I} \cup \mathbb{J})$, is known before the extra squeeze. The second group of equations in (36) is rewritten as

$$(1 + \mu_{\mathcal{F}}^2)(f_{lx} n_{lx} + f_{ly} n_{ly} + f_{lz} n_{lz})^2 = f_{lx}^2 + f_{ly}^2 + f_{lz}^2, \tag{54}$$

After substitutions of (52), the equations in (53) and (54) are quadratic in $u_1, u_2, \ldots, u_\zeta$. The third group of equations in (36) is also quadratic:

$$u_l^2 + u_{l+\eta}^2 = 1, \tag{55}$$

for $l = \xi + 1, \ldots, \xi + \eta$.

The system (53)–(55) consists of ζ quadratic equations in ζ variables. Denote $\boldsymbol{u} = (u_1, \ldots, u_\zeta)^T$, and let the polynomials in the system be $p_1(\boldsymbol{u}), p_2(\boldsymbol{u}), \ldots, p_\zeta(\boldsymbol{u})$.

The homotopy continuation method (Garcia and Zangwill, 1979; Morgan, 1983) is employed to solve the above system. This method can be viewed as a continuous mapping from a known common root of some

"start" system to one of the system of interest, as some control parameter t varies continuously from 0 to 1. The homotopy that we use here is

$$\boldsymbol{H}(\boldsymbol{u},t) = (1-(1-t)^2)\boldsymbol{P}(\boldsymbol{u}) - (1-t)^2\boldsymbol{Q}(\boldsymbol{u}), \tag{56}$$

where

$$\boldsymbol{P} = \begin{pmatrix} p_1(\boldsymbol{u}) \\ p_2(\boldsymbol{u}) \\ \vdots \\ p_\zeta(\boldsymbol{u}) \end{pmatrix} \quad \text{and} \quad \boldsymbol{Q} = \begin{pmatrix} q_1(u_1) \\ q_2(u_2) \\ \vdots \\ q_\zeta(u_\zeta) \end{pmatrix}.$$

It is easy to see that $\boldsymbol{H}(\boldsymbol{u},0) = \boldsymbol{Q}(\boldsymbol{u})$ and $\boldsymbol{H}(\boldsymbol{u},1) = \boldsymbol{P}(\boldsymbol{u})$. To construct the start system $\boldsymbol{Q}$, for example, we may choose $q_i(u_i) = u_i - 1$ or $q_i(u_i) = u_i + 1$, for $i = 1,\ldots,\zeta$, depending on the sliding direction of the corresponding node. Given the simple form of $\boldsymbol{Q}$, the root $\boldsymbol{u}(0)$ of $\boldsymbol{H}(\boldsymbol{u},0) = \boldsymbol{Q}(\boldsymbol{u}) = \boldsymbol{0}$ can be easily determined.

Tracking of the solution $\boldsymbol{u}(t)$ uses the derivative $d\boldsymbol{u}/dt$. We differentiate $\boldsymbol{H}(\boldsymbol{u},t) = \boldsymbol{0}$ with respect to t:

$$\frac{\partial \boldsymbol{H}}{\partial \boldsymbol{u}} \cdot \frac{d\boldsymbol{u}}{dt} + \frac{d\boldsymbol{H}}{dt} = \boldsymbol{0},$$

which yields

$$\frac{d\boldsymbol{u}}{dt} = -\left(\frac{\partial \boldsymbol{H}}{\partial \boldsymbol{u}}\right)^{-1} \frac{d\boldsymbol{H}}{dt}, \tag{57}$$

where $\partial \boldsymbol{H}/\partial \boldsymbol{u}$ is the Jacobian matrix of the form

$$\frac{\partial \boldsymbol{H}}{\partial \boldsymbol{u}} = \begin{pmatrix} \frac{\partial H_1}{\partial u_1} & \frac{\partial H_1}{\partial u_2} & \cdots & \frac{\partial H_1}{\partial u_\zeta} \\ \cdots & \cdots & \cdots & \cdots \\ \frac{\partial H_\zeta}{\partial u_1} & \frac{\partial H_\zeta}{\partial u_2} & \cdots & \frac{\partial H_\zeta}{\partial u_\zeta} \end{pmatrix}.$$

In the above, $\boldsymbol{H} = (H_1,\ldots,H_\zeta)^T$. Next, we obtain the derivative of $\boldsymbol{H}$ with respect to t:

$$\frac{d\boldsymbol{H}}{dt} = (2-2t) \begin{pmatrix} p_1(\boldsymbol{u}) + q_1(u_1) \\ p_2(\boldsymbol{u}) + q_2(u_2) \\ \vdots \\ p_n(\boldsymbol{u}) + q_n(u_n) \end{pmatrix}$$

The homotopy continuation method tracks the root of $\boldsymbol{H}(\boldsymbol{u},t)$ from $t = 0$ to $t = 1$ iteratively with increments of, say, h, starting at $\boldsymbol{u}(0)$, the known root of $\boldsymbol{H}(\boldsymbol{u},0) = \boldsymbol{Q}(\boldsymbol{u})$. In iteration $j+1$, we move from the root $\boldsymbol{u}(jh)$ of $\boldsymbol{H}(\boldsymbol{u},jh) = \boldsymbol{0}$ to the root $\boldsymbol{u}((j+1)h)$ of $\boldsymbol{H}(\boldsymbol{u},(j+1)h) = \boldsymbol{0}$. Write $\boldsymbol{u}_j = \boldsymbol{u}(jh)$ for simplicity. In this iteration, we first obtain

$$\tilde{\boldsymbol{u}}_{j+1} = \boldsymbol{u}_j + h\frac{d\boldsymbol{u}}{dt}(\boldsymbol{u}_j),$$

where $(d\boldsymbol{u}/dt)(\boldsymbol{u}_j)$ is calculated according to (57). The iteration ends with polishing the roots using Newton's method. Let $\boldsymbol{w}_0 = \tilde{\boldsymbol{u}}_{j+1}$ and iterate as follows:

$$\boldsymbol{w}_{k+1} = \boldsymbol{w}_k - \left(\frac{\partial \boldsymbol{H}}{\partial \boldsymbol{u}}(\boldsymbol{w}_k)\right)^{-1} \boldsymbol{H}(\boldsymbol{w}_k). \tag{58}$$

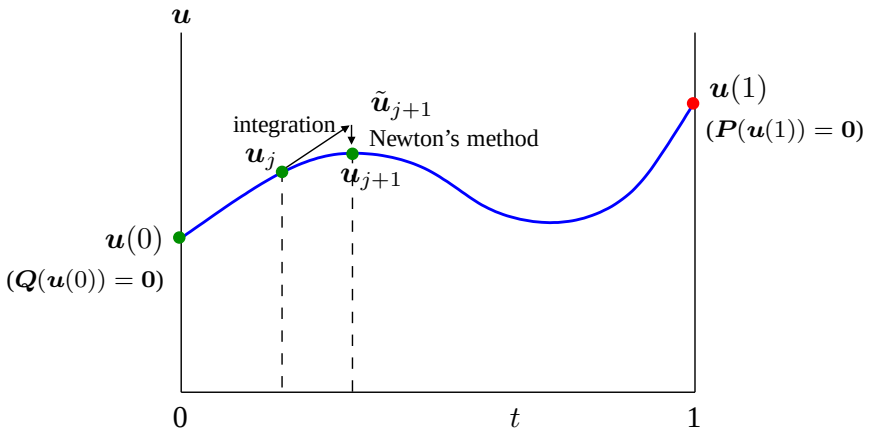

Figure 11: Sliding distances $\boldsymbol{u}(1)$ computed from root tracking using the homotopy continuation method.

Set $\boldsymbol{u}_{j+1}$ to $\boldsymbol{w}_k$ when k is large enough. Figure 11 illustrates how the sliding distances are tracked.

It is known from Section 4 that the system $\boldsymbol{P}(\boldsymbol{u})$ can be set up in $O(\tau^2)$ time, so can $\boldsymbol{H}(\boldsymbol{u}, t)$. During an iteration of the homotopy continuation method, the Jacobian $\partial \boldsymbol{H}/\partial \boldsymbol{u}$ is constructed in $O(\tau^2)$ time. The derivative $d\boldsymbol{H}/dt$ is evaluated in $O(\tau^2)$ time. The Newton's method carries out each iteration according to (58) in $O(\tau^3)$ time due to the Jacobian inversion. Given the quadratic convergence of the Newton's method, it is reasonable to assume that it iterates a constant number of times to polish $\boldsymbol{u}_{j+1}$. The homotopy continuation method takes $r = 1/h$ iterations to reach $t = 1$. Its execution time is thus $O(r\tau^3)$.

D Sliding Effect and Error Bounding

Slip estimation is the main reason for the contact update described in Section 4 to be expensive. Computation would be greatly reduced if every contact node could be simply treated as "sticking". But how much error could result then?

Meanwhile, errors in the estimates of the changing contact configuration will propagate and accumulate, since Algorithm 1 is iterative. This could create a large enough difference between the estimate and the real configuration such that the liftability test is passed prematurely leading to a pickup failure.

To address the above issues, let us first rewrite (11) for the displacement vector via substitutions of (22) and (23):

$$\boldsymbol{\Delta} = V \left(D(\bar{\boldsymbol{\Delta}} - \bar{\boldsymbol{c}}) + \frac{w_0}{\sqrt{n}} \boldsymbol{Q} - L^T \boldsymbol{F}_0 \right), \tag{59}$$

where

$$D = \begin{pmatrix} \bar{\boldsymbol{v}}_1^T C/\lambda_1 \\ \vdots \\ \bar{\boldsymbol{v}}_{3n-6}^T C/\lambda_{3n-6} \\ E^T \end{pmatrix}, \tag{60}$$

$$\boldsymbol{Q} \;=\; \begin{pmatrix} \bar{\boldsymbol{v}}_1^T \boldsymbol{e}_3/\lambda_1 \\ \vdots \\ \bar{\boldsymbol{v}}_{3n-6}^T \boldsymbol{e}_3/\lambda_{3n-6} \\ \boldsymbol{h}_3 \end{pmatrix},$$

and $L = (\boldsymbol{v}_1/\lambda_1, \ldots, \boldsymbol{v}_{3n-6}/\lambda_{3n-6}, \mathbf{0})$.

Between two contact events, the set of contact nodes does not vary. So, the matrix D and the vectors $\bar{\boldsymbol{c}}$ and $\boldsymbol{Q}$ are constant. Suppose the estimate of the contact displacement vector $\bar{\boldsymbol{\Delta}}$ is off by $\delta\bar{\boldsymbol{\Delta}}$ due to ignorance of all contact slips during the period. The predicted shape will change by

$$\delta\boldsymbol{\Delta} = VD \cdot \delta\bar{\boldsymbol{\Delta}}.$$

Take the 2-norm of both sides of the above equation:

$$\begin{aligned} \|\delta\boldsymbol{\Delta}\|_2 &= \|VD \cdot \delta\bar{\boldsymbol{\Delta}}\|_2 \\ &\leq \|VD\|_2 \cdot \|\delta\bar{\boldsymbol{\Delta}}\|_2 \\ &= \sigma_{\max}(VD) \cdot \|\delta\bar{\boldsymbol{\Delta}}\|_2, \end{aligned}$$

where $\sigma_{\max}(VD)$ is the largest singular value of VD, i.e. the square root of the largest eigenvalue of $D^T V^T VD = D^T D$. From (60) we obtain

$$D^T D = CA'C + EE^T, \tag{61}$$

where $A' = \sum_{k=1}^{3n-6} \bar{\boldsymbol{v}}_k \bar{\boldsymbol{v}}_k^T/\lambda_k^2$ is very similar to the matrix A defined in (15). The matrix A' depends on the current contact set. We see that $\sigma_{\max}(VD)$ gives the worst-case magnification of an error in the contact estimate to an error in the deformation estimate at the current contact configuration.

How to bound $\|\delta\bar{\boldsymbol{\Delta}}\|_2$? The relative sliding of a boundary node is indicated by the strain at its current position along the sliding direction. We can evaluate this strain from the six principal strains $\epsilon_x, \epsilon_y, \epsilon_z, \gamma_{xy}$, γ_{xz}, γ_{yz} by transforming them (Sadd, 2009, pp. 38–40) to a new coordinate system with one principal axis aligned with the sliding direction.

Figure 12 shows an intermediate configuration (at $\rho = 0.022$) of the two fingertips squeezing an object with the shape of the steamed bun shown in Table 1. Let relevant geometric and physical parameters assume the same values listed for the bun in Table 2 but set $E = 5 \times 10^4$ and $\mu_{\mathcal{F}} = \mu_{\mathcal{P}} = 0.3$. For better illustration, the initial finger placement differs from that on the bun in Table 3. There are 14 nodes in contact with the left fingertip, 13 with the right fingertip, and 25 on the plane.

The maximum sliding distance of any node is 3.24%.[13] It is close to the strain 0.033 at the maximizing node along the sliding direction. In the worst case, $\|\delta\bar{\boldsymbol{\Delta}}\|_2$ is $0.033\sqrt{m}$, where τ is the number of contact nodes. This bounds the contact error due to ignorance of slips in the current period between two contact events. Meanwhile, based on the current contact configuration, we calculate

$$\sigma_{\max}(VD) = 10.33 \qquad \text{and} \qquad \frac{\|\delta\boldsymbol{\Delta}\|_2}{\|\delta\bar{\boldsymbol{\Delta}}\|_2} = 3.80.$$

During the same period the worst-case error $0.033\sqrt{m}$ could be magnified 3.8 to 10.33 times in the object's deformation. Such errors, accumulating over all periods, may grow significant enough to cause an erroneous prediction by the liftability test that is large enough to lead to a pickup failure.

[13] The result was computed relative to the neighboring node that lies in a direction that is closest to the sliding direction.

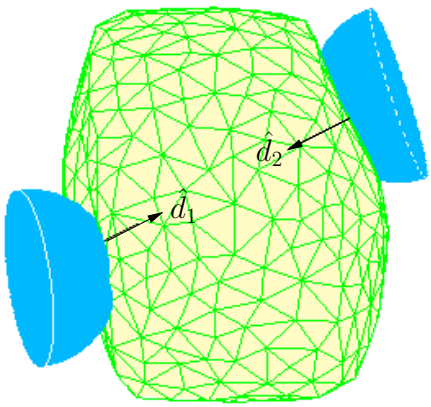

Figure 12: Intermediate configuration of squeezing a bun-like object.

E Minimum Normal Force to Pick up a Rigid Body

The analysis in this appendix supplements the comparison with rigid body grasping in Section 7. Consider two fingers making point contacts with a rigid body of mass m to lift it up through an equilibrium grasp. The effort by the grasping fingers is best measured by the total normal force they exert. In this section, we minimize such effort.

Suppose that the two fingers are in contact with the object at $\boldsymbol{p}_1 = (x_1, y_1, z_1)^T$ and $\boldsymbol{p}_2 = (x_2, y_2, z_2)^T$ with unit inward normals $\hat{\boldsymbol{n}}_1$ and $\hat{\boldsymbol{n}}_2$, respectively. The fingers exert forces $\boldsymbol{f}_1$ and $\boldsymbol{f}_2$ at the contact points, respectively.

Without loss of generality, let the object's center of mass be at the origin. Force and torque equilibria are described by the following equation:

$$\begin{pmatrix} 1 & 0 & 0 & 1 & 0 & 0 \\ 0 & 1 & 0 & 0 & 1 & 0 \\ 0 & 0 & 1 & 0 & 0 & 1 \\ 0 & -z_1 & y_1 & 0 & -z_2 & y_2 \\ -x_1 & 0 & z_1 & -x_2 & 0 & z_2 \\ -y_1 & x_1 & 0 & -y_2 & x_2 & 0 \end{pmatrix} \begin{pmatrix} \boldsymbol{f}_1 \\ \boldsymbol{f}_2 \end{pmatrix} = \begin{pmatrix} 0 \\ 0 \\ -mg \\ 0 \\ 0 \\ 0 \end{pmatrix}. \tag{62}$$

The least effort problem can be formulated below:

$$\begin{aligned} \text{Minimize} \quad & \boldsymbol{f}_1 \cdot \hat{\boldsymbol{n}}_1 + \boldsymbol{f}_2 \cdot \hat{\boldsymbol{n}}_2 \\ \text{Subject to} \quad & (62) \\ & \left(\frac{\boldsymbol{f}_1 \cdot \hat{\boldsymbol{n}}_1}{\|\boldsymbol{f}_1\| \|\hat{\boldsymbol{n}}_1\|} \right)^2 \geq \frac{1}{1+\mu_{\mathcal{F}}^2} \\ & \left(\frac{\boldsymbol{f}_2 \cdot \hat{\boldsymbol{n}}_2}{\|\boldsymbol{f}_2\| \|\hat{\boldsymbol{n}}_2\|} \right)^2 \geq \frac{1}{1+\mu_{\mathcal{F}}^2} \\ & \boldsymbol{f}_1 \cdot \hat{\boldsymbol{n}}_1 \geq 0 \\ & \boldsymbol{f}_2 \cdot \hat{\boldsymbol{n}}_2 \geq 0 \end{aligned} \tag{63}$$

The last four constraints above ensure that the finger contact forces are compressive and lie inside their respective friction cones.

First, we eliminate constraint (62). In its 6×6 coefficient matrix, for $k = 1, 2, 3$ we subtract column k from column $k+3$ to zero out the upper right 3×3 submatrix. In the obtained matrix, we subtract multiples of the first three rows from the last three rows to zero out the lower left 3×3 submatrix. The lower right 3×3 matrix after these operations becomes

$$\begin{pmatrix} 0 & z_1 - z_2 & y_2 - y_1 \\ x_1 - x_2 & 0 & z_2 - z_1 \\ y_1 - y_2 & x_2 - x_1 & 0 \end{pmatrix}.$$

It has zero determinant and rank 2 since $\boldsymbol{p}_1 \neq \boldsymbol{p}_2$. The coefficient matrix in (62) thus has rank 5. In fact, any five of its six rows are linearly independent. We infer that the six components of $\boldsymbol{f}_1$ and $\boldsymbol{f}_2$ have one dependency. These components can be uniquely determined from (62) in terms of one component, say, f_{1x}, the x-component of $\boldsymbol{f}_1$.

After substitutions of the linear expressions of f_{1x} for $\boldsymbol{f}_1$ and $\boldsymbol{f}_2$, the constraint (62) is eliminated and the optimization problem (63) is transformed into

$$\begin{aligned} \text{Minimize} \qquad & cf_{1x} + d & & & (64) \\ \text{Subject to :} \ & a_1 f_{1x}^2 + b_1 f_{1x} + c_1 & \geq & 0 & (65) \\ & a_2 f_{1x}^2 + b_2 f_{1x} + c_2 & \geq & 0 & (66) \\ & d_1 f_{1x} + e_1 & \geq & 0 & (67) \\ & d_2 f_{1x} + e_2 & \geq & 0 & (68) \end{aligned}$$

Proposition 6 *At least one of $\boldsymbol{f}_1$ and $\boldsymbol{f}_2$ that minimize (64) under the constraints (65)–(68) must lie on an edge of its corresponding friction cone; namely, either (65) or (66) becomes an equality at the minimum.*

Proof Each of the constraints (65)–(68) is satisfied over up to two intervals of $\mathbb{R}$, whose endpoints are either the two infinity points or the roots of the corresponding equality constraint. Intersection of all such intervals yields a sequence of intervals in the form of $[a, b]$, $[a, \infty)$, or $(-\infty, b]$, over which the constraints (65)–(68) are all satisfied. Since the objective function (64) is linear, the minimum must be achieved at an endpoint of one of the intervals in the sequence.

The minimum total normal force, in its original form (63) under the constraints (62), $\boldsymbol{f}_1 \cdot \hat{\boldsymbol{n}}_1 \geq 0$, and $\boldsymbol{f}_2 \cdot \hat{\boldsymbol{n}}_2 \geq 0$, is apparently non-negative. This carries over to the minimum value of the equivalent form (64) under the constraints (67) and (68). If $c > 0$, the minimizing f_{1x} must be a left endpoint that is not $-\infty$, otherwise the minimum value would become negative. Neither can it be ∞, which may only be a right endpoint. Similarly, if $c < 0$, the minimizing f_{1x} can be neither $-\infty$ nor ∞. Still two possible cases remain:

1. The minimum is achieved at a root of the quadratic equality induced from (65) or (66). This means that $\boldsymbol{f}_1$ or $\boldsymbol{f}_2$ lies on a friction cone edge.

2. The minimum is achieved at a root of the linear equality induced from (67) or (68), or equivalently, when $\boldsymbol{f}_1 \cdot \hat{\boldsymbol{n}}_1 = 0$ or $\boldsymbol{f}_2 \cdot \hat{\boldsymbol{n}}_2 = 0$. Only one finger is active. It must be placed vertically below the object's center of mass. This is not the two-finger grasping scenario considered by us.

The proposition follows from case 1. □